

Review

# Ultra-Low Cycle Fatigue Life Prediction Model—A Review

Yali Xu, Xin Li \* , Yanjuan Zhang  and Jianwei Yang

School of Mechanical-Electronic and Vehicle Engineering, Beijing University of Civil Engineering and Architecture, Beijing 100044, China; 2108550021125@stu.bucea.edu.cn (Y.X.); zhangyanjuan@bucea.edu.cn (Y.Z.); yangjianwei@bucea.edu.cn (J.Y.)

\* Correspondence: lixin0301@bucea.edu.cn; Tel.: +86-186-1085-6280

**Abstract:** This article is a review of models for predicting ultra-low cycle fatigue life. In the article, the life prediction models are divided into three types: (1) microscopic ductile fracture models based on cavity growth and cavity merger; (2) fracture models based on porous plasticity; and (3) ductile fracture models based on continuum damage mechanics. Furthermore, the article provides a critical assessment of the current state of research on ultra-low cycle fatigue life prediction models, highlighting the limitations and challenges faced by each model type. Ultimately, this review aims to provide a comprehensive overview of the different models available for predicting ultra-low cycle fatigue life and to guide future research in this important area of materials science and engineering.

**Keywords:** ultra-low cycle fatigue; failure mechanism; life prediction models; microstructure evolution; development direction

## 1. Introduction

In general, fatigue damage in structural steel can be classified as low-cycle fatigue ( $N_f = 10^4 \sim 10^5$ ), high-cycle fatigue ( $N_f = 10^5 \sim 10^7$ ), and ultra-high-period fatigue ( $N_f > 10^7$ ) [1]. However, when structures are subjected to large strain loading cycles, failure occurs in a very short number of cycles (typically between a few and several hundred cycles) [2]. Strong earthquakes last usually for about 1 min, the amplitude-frequency is usually 1 to 3 Hz, and damage to buildings occurs within 100 to 200 cycles [3,4]. As shown in Figure 1, this fatigue failure under the action of fewer cycles ( $N_f < 100$ ) is called “ultra-low cycle fatigue (ULCF)”.

The emphasis on ULCF in the field of structural engineering emerged as a response to the 1994 Northridge earthquake in the United States and the 1995 Kobe earthquake in Japan. Research conducted following these earthquakes showed that post-earthquake building damage was caused by fatigue fractures that occurred under fewer cycles and larger plastic strains, which exhibited different fracture surfaces compared to ordinary fatigue (as illustrated in Figure 2).

Although research efforts have been made to optimize building structures and develop new earthquake-resistant methods, there has been relatively less focus on the problem of ULCF failure in structural steel. However, with the increasing use of steel structures in high-rise buildings and bridges, addressing the issue of ULCF in steel structures has become an urgent and critical challenge that requires attention. Further research is necessary to develop effective strategies for addressing ULCF in structural steel and ensuring the safety and reliability of steel structures [5].



**Citation:** Xu, Y.; Li, X.; Zhang, Y.; Yang, J. Ultra-Low Cycle Fatigue Life Prediction Model—A Review. *Metals* **2023**, *13*, 1142. <https://doi.org/10.3390/met13061142>

Academic Editors: Alberto Campagnolo and Alberto Sapora

Received: 15 May 2023

Revised: 10 June 2023

Accepted: 14 June 2023

Published: 19 June 2023



**Copyright:** © 2023 by the authors. Licensee MDPI, Basel, Switzerland. This article is an open access article distributed under the terms and conditions of the Creative Commons Attribution (CC BY) license (<https://creativecommons.org/licenses/by/4.0/>).

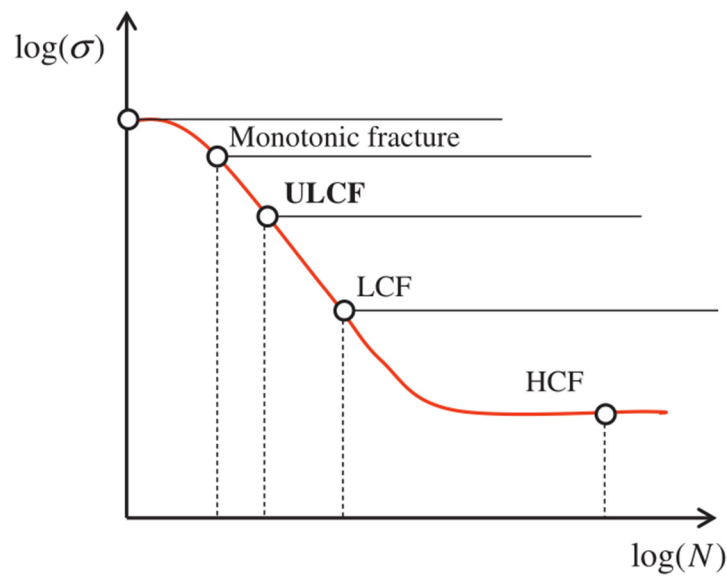


**Figure 1.** Relation of ULCF with other damage mechanisms. Reprinted with permission from Ref. [6]. 2014, Elsevier.

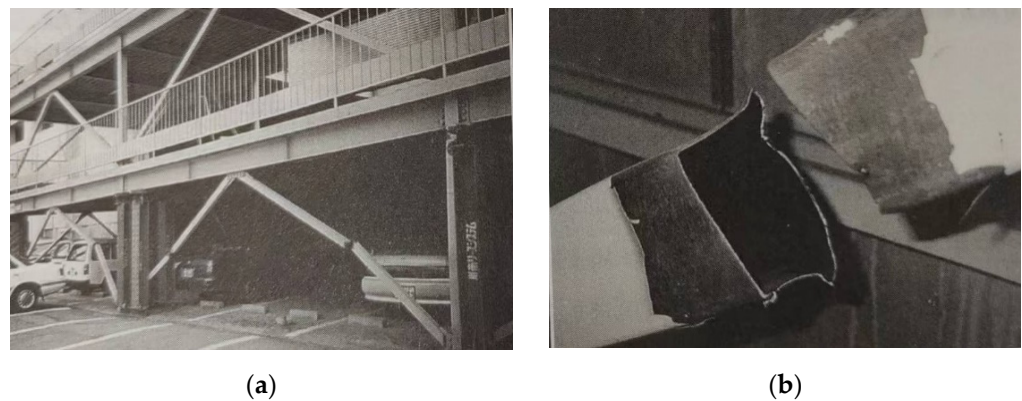


**Figure 2.** Ductile fracture of bracing structure in the 1995 Kobe earthquake. (a) bracing structure, (b) fracture area. Reprinted with permission from Ref. [7]. 2018, Tongji University Press.

ULCF typically involves a high magnitude of plastic strain, which can result in significant plastic deformation of the material being tested. This is due to the high strain amplitudes associated with ULCF, which can cause the material to undergo large deformations with each cycle. In contrast, LCF typically involves a lower magnitude of plastic strain than ULCF. While plastic deformation still occurs in LCF, the strain amplitudes are generally lower than those associated with ULCF. This means that the plastic deformation that occurs in the material during LCF is typically less severe than that observed in ULCF [8–11]. The fracture initiation and propagation zones of ordinary fatigue fracture are mainly characterized by transgranular cleavage, showing characteristics similar to brittle fracture; the fracture of ULCF has a large number of deep dimples, showing characteristics of ductile fracture (Figure 3) [12]. It can be seen that there are obvious differences between the damage mechanisms of ULCF and ordinary fatigue. The damage mechanisms associated with ULCF are complex and can involve a combination of plastic deformation, cracking, void formation, and other types of microstructural changes. The specific damage mechanism that occurs in a given material depends on a range of factors, including the material properties, the loading conditions, and the number of cycles [13]. If the low-cycle fatigue analysis method is applied to deal with the problem, it will produce large errors. Similarly, applying the theory of plastic fracture to metal structures under monotonic

loading cannot obtain satisfactory results. Therefore, further research on the mechanisms of crack initiation, extension, and fracture is needed.

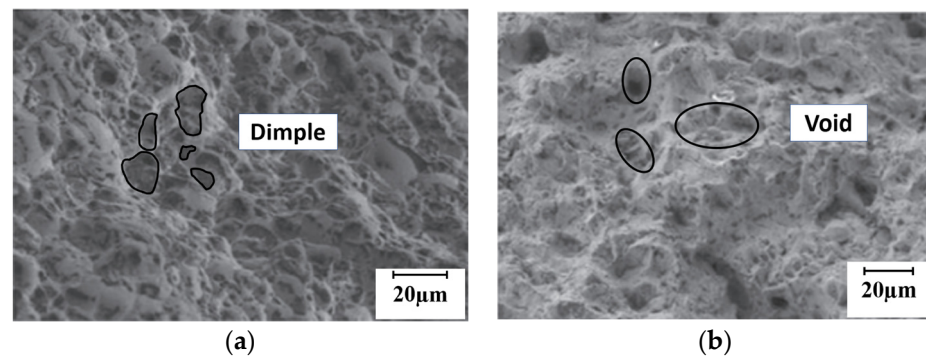


**Figure 3.** The morphology of the ULCF of the Q235 specimen was observed under SEM: (a) monotonic tensile loading, (b) ultra-low cyclic loading. Reprinted with permission from Ref. [14]. 2020, Elsevier.

Due to the typical ductile fracture characteristics of structural steel in ULCF, the investigation of ductile fracture mechanisms has become a fundamental aspect of ULCF research. Over the past half-century, researchers have developed three types of ductile fracture models, which have emerged gradually: (1) microscopic ductile fracture models based on cavity growth and cavity merger; (2) fracture models based on porous plasticity; and (3) ductile fracture models based on continuum damage mechanics. During the process of ULCF development, many methods for predicting fatigue life have been proposed. In response to these studies, many experts have applied and improved models, and the parameters and results of the fitting of the life prediction model have been calibrated through experiments and simulations.

## 2. Improved Manson-Coffin Model

The Manson-Coffin model [15,16] is an empirical formula for analyzing the low-cycle fatigue life of steel under the action of thermal stress. Equation (1) is:

$$\Delta\varepsilon_p(2N_f)^k = C \quad (1)$$

The cumulative damage under cyclic loading is calculated according to Miner's rule [17]. The equation for the damage index  $D$  is Equation (2):

$$D = \sum D_i = \sum \left( \frac{n_i}{N_{fi}} \right) = 1 \quad (2)$$

The damage index  $D$  is equal to zero when there is no damage and is equal to unity when a ULCF fracture occurs.

In these papers [18–20], the Manson-Coffin empirical law states that the cycle life before crack initiation decreases as the plastic strain amplitude increases. This relationship between crack initiation life and plastic strain amplitude has been determined through cyclic loading tests. However, it has been discovered that the cracks generated under ultra-low-cycle loading are not fatigue cracks, but rather ductile. As a result, the Coffin-Manson relationship cannot be directly applied to the ultra-low-cycle fatigue field. These findings highlight the need for further research to develop more accurate models that can account for the unique characteristics of ULCF in structural steel.

Xue [21,22] extended the Coffin-Manson law for life prediction under ULCF by introducing an exponential function. The new expression is Equation (3):

$$\Psi \left( \frac{\Delta\varepsilon_d}{\varepsilon_f} \right) = \frac{e^{\lambda \left( \frac{\varepsilon_d}{\varepsilon_f} \right)^m} - 1}{e^\lambda - 1} \quad (3)$$

The damage rate is derived from Equation (4) is:

$$dD = \frac{m\lambda \left(\frac{\varepsilon_d}{\varepsilon_f}\right)^{(m-1)} e^{\lambda \left(\frac{\varepsilon_d}{\varepsilon_f}\right)^m}}{e^\lambda - 1} \frac{d\varepsilon_p}{\varepsilon_f} \quad (4)$$

where  $m = 1.37$  and  $\lambda = 3.85$ . When  $D = 1$ , the material fractures.

It should be noted that in the study mentioned, the author only tested smooth specimens without taking into account the effects of stress triaxiality and load parameters. To address this limitation, Pereira et al. [23] introduced stress triaxiality and load parameters and conducted cyclic pure bending tests on full-scale pipes used in industrial pipelines. Small-scale smooth specimens were also used for support and finite element simulations. The results obtained from these tests were found to be more accurate in predicting the behavior of ULCF in structural steel.

Li et al. [12] proposed a modified Coffin-Manson model that incorporates stress triaxiality and established an empirical equation between model parameters and stress triaxiality, as shown in Equation (5), based on ULCF test results.

$$\Delta\varepsilon_{eq}(2N_f)^{k(T)} = C(T) \quad (5)$$

To verify the applicability of the proposed model, Q345qC steel specimens with different radius notches (as shown in Figure 4) were subjected to four different cyclic loadings. In ULCF studies, specimens with different notch radii are typically used to represent different levels of triaxial stress conditions. The gauge length of the extensometer is 50 mm. Strain-controlled loading is used, and the specimens are tested under four different cyclic loading conditions. As shown in Figure 5a constant reversal cyclic loading is applied; (2) one cycle reversal cyclic loading at each strain range and  $1.0 \varepsilon_y$  incremental per one cycle; (3) three cycles reversal cyclic loading at each strain range and  $1.0 \varepsilon_y$  incremental per three cycles; (4) relative arbitrary loading form is applied. The segmented calibration method under different average stress triaxialities was used to determine the relationship between model parameters and stress triaxialities. The Coffin-Manson model, which takes into account stress triaxiality, was validated through experimentation and simulation. It demonstrated a reasonable prediction accuracy of 12.5% across varying stress triaxialities. This can improve the accuracy of ultra-low-cycle fatigue predictions.

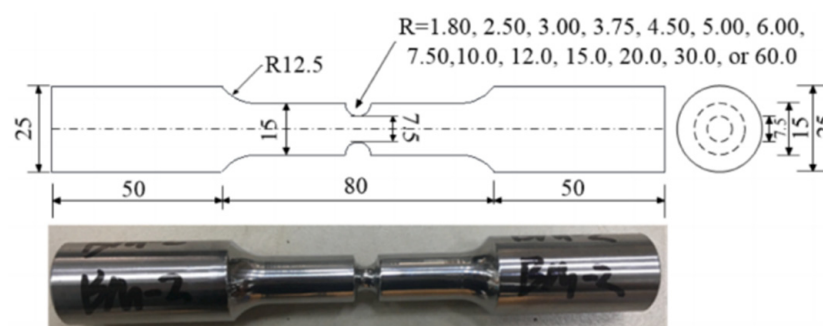


**Figure 4.** The notched specimen under cyclic loading. Reprinted with permission from Ref. [12]. 2020, Elsevier.

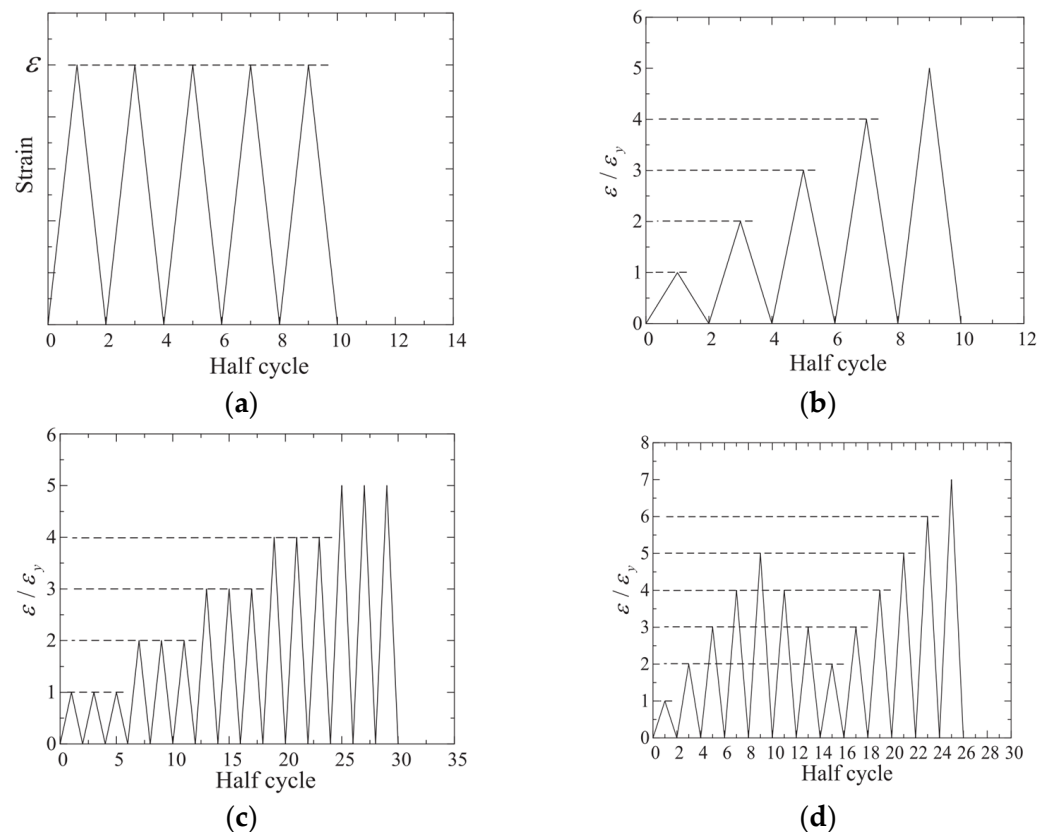


**Figure 5.** Loading protocol for cyclic loading. (a) constant reversal cyclic loading. (b) one cycle reversal cyclic loading. (c) three cycles reversal cyclic loading. (d) relative arbitrary loading. Reprinted with permission from Ref. [12]. 2020, Elsevier.

Although the improved Coffin-Manson model has higher prediction accuracy than the previous model [12]. The significant difference in fracture mechanisms between low-cycle fatigue and ULCF still requires further exploration of the improved model. During the research process at ULCF, various methods and theories have emerged, leading to continuous innovations over time.

### 3. Microcosmic Ductility Fracture Model Based on Void Growth

In the study of the material microstructure morphology evolution during ductile fracture, it is believed that ductile fracture of metals usually involves three key stages [17]: (1) the formation of void nuclei by interfacial stripping or particle rupture of impurities or second-phase particles; (2) the continuous growth of void under the combined influence of equivalent plastic strain and hydrostatic pressure; and (3) the merging of void when they increase to a critical size, as shown in Figure 6. Based on their studies of the ductile fracture process of metals, researchers have proposed various ductile fracture models based on void growth.

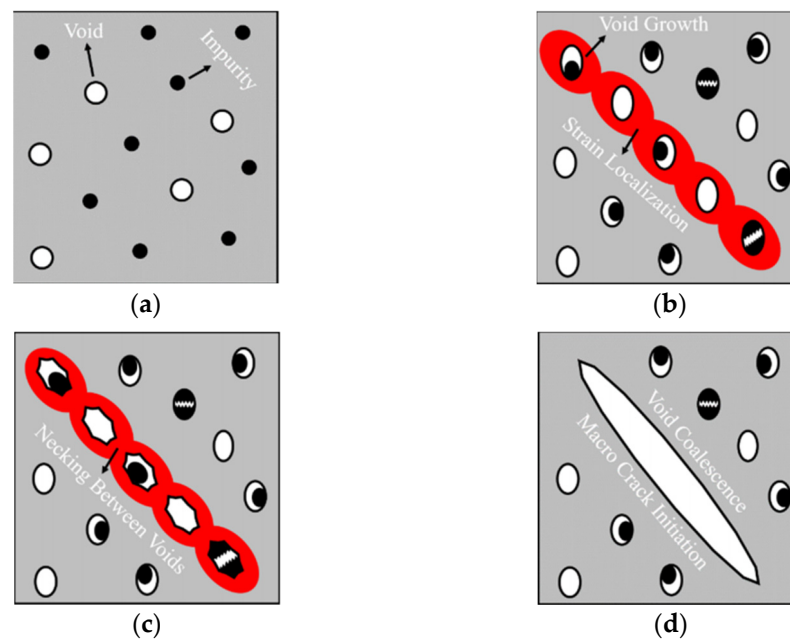


**Figure 6.** Ductile fracture mechanisms in metals: (a) Void Nucleation; (b) Void Growth and Strain Localization; (c) Necking between Voids; (d) Void Coalescence and Macroscopic Crack Initiation. Reprinted with permission from Ref. [24]. 2020, Elsevier.

Mcclintock [25,26] proposed a ductile fracture initiation criterion that is based on the analysis of the growth of cylindrical voids in a plastic deformation matrix under a far-field plane strain field for the first time.

### 3.1. Rice-Tracey Model

Rice and Tracey [27] established the relationship between cavity radius and stress tri-axiality through mechanical analysis of spherical cavities subjected to far-field simple tensile strain rate fields. They also proposed a model for cavity growth rate and stress triaxiality correlation, which can be approximated by Equation (6) for Mises materials.

$$\frac{dR}{R} = ae^{bT} d\epsilon_{eq} \quad (6)$$

where  $a = 0.283$ ,  $b = 1.5$  are the material constants.

The study has revealed that hydrostatic pressure plays a vital role in the growth of microvoids, and an increase in stress triaxiality leads to a rapid decrease in the fracture strain of the material. This groundbreaking discovery highlights the correlation between void growth rate, stress triaxiality, and strain rate. However, this theory only applies to the ductile fracture problem of materials with a single void and does not offer criteria for their merging when multiple voids are present. Devaux addressed this limitation by replacing the yield stress with von Mises equivalent stress and introducing the renowned Void Growth Model (VGM) fracture model. In most practical engineering scenarios, stress triaxiality remains relatively constant.

Mortezaghali et al. [24] verified the above VGM model and applied it to the cyclic behavior of double-core buckling restrained braces (BRBs). To further determine the crack initiation time, specimens made of all-steel BRB were used to verify the simulation results. The criterion for crack initiation is given by Equation (7).

$$\eta = \int d\eta = \int \frac{d\epsilon_{eq}^p}{\epsilon_{fr}(T)} = 1 \quad (7)$$

As shown in Figure 7, it reflects the cumulative damage to the specimen during the loading process. According to Equation (7), it can be calculated that when  $\eta = 1$ , the material undergoes crack initiation. Crack propagation occurs rapidly and eventually leads to fatigue failure.

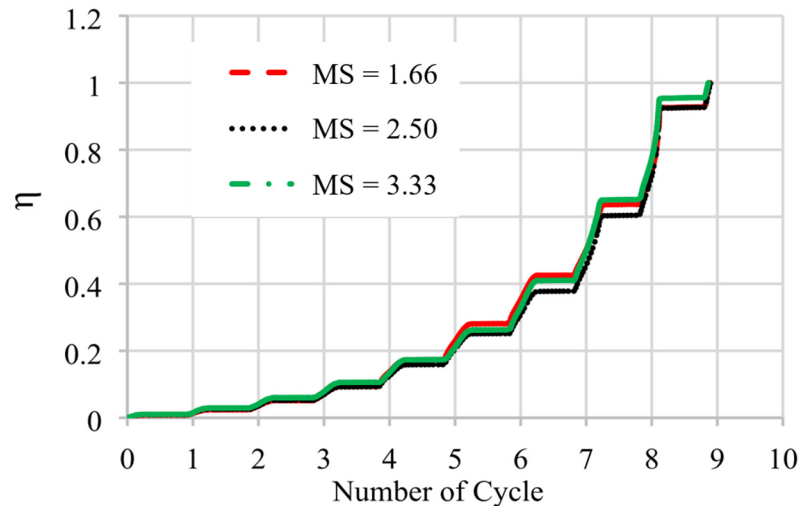


Figure 7. Crack initiation criteria. Reprinted with permission from Ref. [24]. 2020, Elsevier.

### 3.2. The Micromechanical Void Growth Model (MM-VGM)

According to [28], the void growth model (VGM) is insufficient for predicting porosity growth in strain-hardening metals under monotonic loading, and requires optimization through micromechanical analysis. To predict ULCF life, a new micromechanical cyclic void growth model (MM-VGM) has been proposed, which takes into account the relative change in micro-void volume with macroscopic and microscopic state variables. In Figure 8, the researchers selected a cylindrical region with an embedded spherical void as the computational unit to investigate the growth of micropores under external stress conditions. The fracture criterion can be expressed as a damage integral in Equations (8) and (9):

$$d_{int}(\epsilon_{eff}, T_\sigma) = \int_0^{\epsilon_{eff}} (1.7 \ln(T_\sigma) + 2.5) d\epsilon_{eff} > \int_0^{f_R} df_R = d_{cr} \tag{8}$$

$$overlength \geq l^* \tag{9}$$

In finite element analysis, a cylindrical domain with an embedded spherical void is selected as the computational unit, and the initial geometry of the computational unit is described by the aspect ratios of the unit’s length and width  $\lambda_{c0}$ , the aspect ratio of the void  $\lambda_{v0}$ , and the void volume fraction  $f_0$  as Equations (10)–(12):

$$\lambda_{c0} = \frac{l_{z0}}{l_{r0}} \tag{10}$$

$$\lambda_{v0} = \frac{r_{z0}}{r_{r0}} \tag{11}$$

$$f_0 = \frac{\text{Initial void volume}}{\text{Initial cell volume}} = \frac{2r_{r0}^2 r_{z0}}{3l_{r0}^2 l_{z0}} \tag{12}$$

In finite element analysis, the initial void volume fraction of the material is set to  $f_0 = 0.01$ , and the variation of the void volume fraction is obtained under different triaxial stresses. As shown in Figure 9, When the initial volume fraction of voids is the same, the volume fraction of voids increases with increasing triaxial stress. When  $T_\sigma \leq 1$ , the volume

fraction of voids varies linearly with macroscopic strain. When  $T_\sigma \geq 1$ , the volume fraction of voids increases nonlinearly.

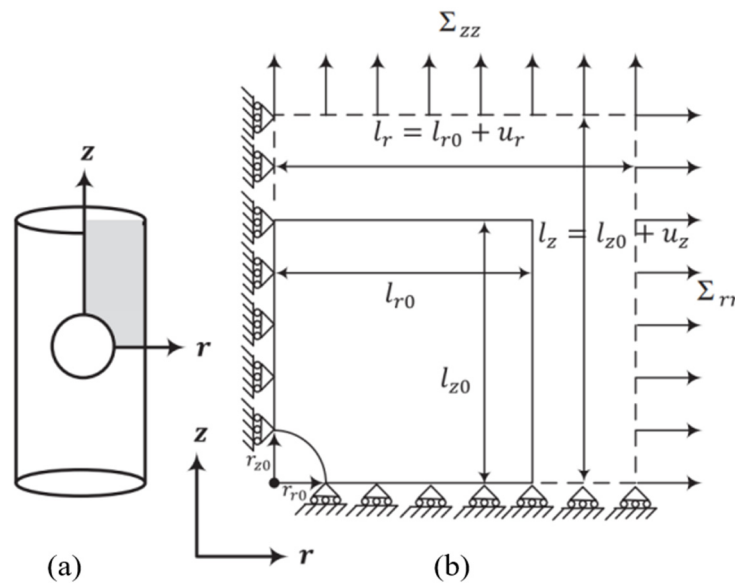


**Figure 8.** (a) Cylindrical RVE with an embedded spherical void, (b) computational cell model with applied boundary conditions:  $u_r$  and displacement fields in  $r$  and  $z$  directions, respectively. Reprinted with permission from Ref. [28]. 2013, Elsevier.

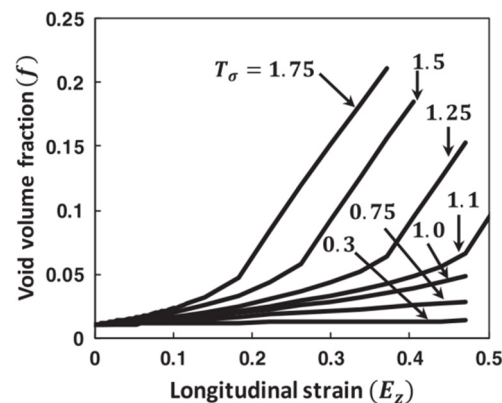


**Figure 9.** Void volume fraction ( $f$ ) versus macroscopic strain in the  $z$ -direction ( $E_z$ ) for varying stress triaxialities in ASTM A992 steels ( $f_0 = 0.001$ ). Reprinted with permission from Ref. [28]. 2013, Elsevier.

Figure 10 shows the influence of the initial volume fraction of voids on the volume fraction of voids ( $f$ ) under three different levels of triaxial stress. It can be seen from Figure 10 that the volume fractions of voids increases with increasing initial volume fraction of voids, and this trend becomes more pronounced under high levels of triaxial stress.

The authors validated the ability of MM-VGM to predict crack initiation. They conducted monotonic tensile tests on specimens with varying notch radii to simulate the strain at crack initiation under different triaxial stress levels, as illustrated in Figure 10. The point on the displacement-load curve where the load-carrying capacity suddenly drops is considered the beginning of crack initiation.

Although the prediction accuracy of the above two models is considerable, the fatigue fracture of structural steel under ULCF loading cannot be predicted well under strong earthquakes. Therefore, on this basis, the model is improved and applied to the fatigue problem in the cyclic loading protocol [29].

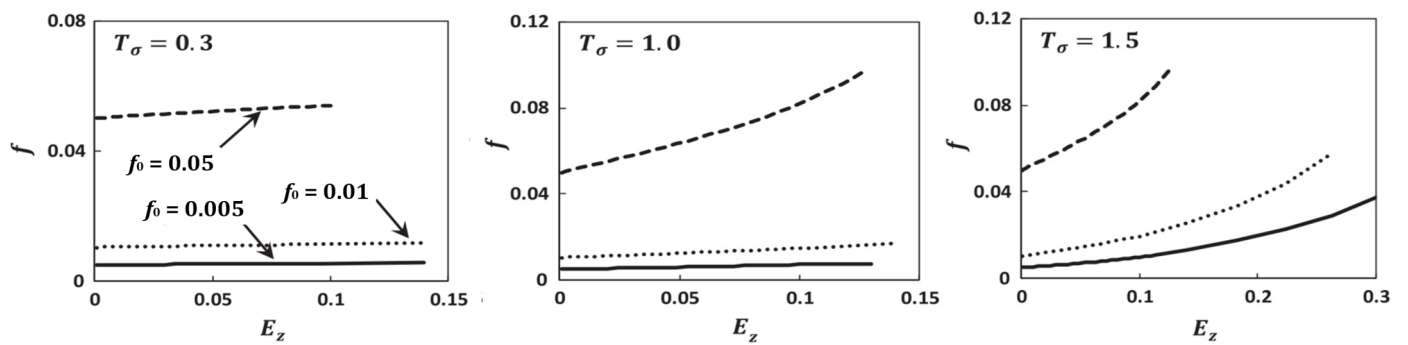


**Figure 10.** Void volume fraction ( $f$ ) versus macroscopic strain in the  $z$ -direction ( $E_z$ ) for different initial void volume fractions ( $f_0$ ) at different stress triaxialities in ASTM A992 steels. Reprinted with permission from Ref. [28], 2013, Elsevier.

### 3.3. Stress-Modified Critical Strain (SMCS) Model

Hancock and Mackenzie [30] first proposed the semi-empirical stress-modified critical strain (SMCS) model (Equation (13)). SMCS is easier to apply than VGM and only depends on the plastic strain. It is suitable for scenarios where stress triaxiality remains relatively constant throughout the loading process [31].

$$\varepsilon_p^{\text{critical}} = \alpha \exp\left(-1.5 \frac{\sigma_m}{\sigma_e}\right) \quad (13)$$

The  $\alpha$  representative material parameters can be determined through experiments, similar to the critical cavity growth index. The calculation method for Equation (14) is as follows:

$$\alpha = \varepsilon_p^{\text{critical}} \cdot \exp\left(-1.5 \frac{\sigma_m}{\sigma_e}\right) \quad (14)$$

Different bar specimens with different notch radii were used to obtain different stress triaxialities, with smaller notch radii corresponding to higher stress triaxialities. However, experimental studies showed that the values obtained from each bar specimen with the same notch radius were very similar, indicating a low dependence on the critical plastic strain and stress triaxiality. The influence of characteristic length was also considered. The mean value of  $l^*$  was the average length of ten plateaus and troughs. The upper bound was the length of the largest plateau or trough. The lower bound was twice the average diameter of the dimple. Figure 11 is a fractography.

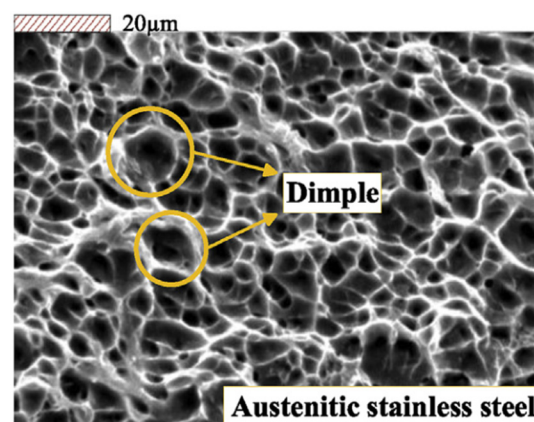


**Figure 11.** A dimple is used as a measure of characteristic length. Reprinted with permission from Ref. [32], 2019, Elsevier.

Meanwhile, there are similarities in the crack initiation criteria between these two models. The associated fracture initiation criteria for the VGM and SMCS can be written as Equations (15) and (16):

$$VGI > VGI_{critical} \text{ over } r > l^* \tag{15}$$

$$\epsilon_p > \epsilon_p^{critical} \text{ over } r > l^* \tag{16}$$

When the above conditions are met, the material will experience crack initiation.

Myers et al. [33] studied the parameter size effect and empirical identification method of the stress-modified critical strain (SMCS) model. Through repeated testing on three notched specimen types made of two different materials, it was found that the toughness parameters were relatively insensitive to calibration specimen size. Yin et al. [34] conducted experiments on the base metal, heat-affected zone, and weld metal of Q460C HSS, and calibrated the toughness parameters of VGM, SMCS, and CVGM (Cyclic Void Growth Model) by fitting the results to the experiments. The specimens were taken from the base metal (BM), weld metal, and heat-affected zone (HAZ) of the high-strength steel welded plate, respectively. The specimens taken from the weld metal were obtained from both the rolling direction (WT) and the perpendicular rolling direction (WL). Chang and Luo [35,36] also calibrated the fracture toughness parameters of S220503 duplex stainless steel under VGM, SMCS, and CVGM (Table 1).

**Table 1.** Micromechanical model parameters. Reprinted with permission from Ref. [33]. 2010, American Society of Civil Engineers.

Steel	$E$ Gpa	$\sigma_y$ (MPa)	$\sigma_u$ (MPa)	$\frac{\sigma_u}{\sigma_y}$	Z/%	A/%	$\eta$	$\lambda_{CVGM}$	$l^*$ Lower (mm)	$l^*$ Mean (mm)	$l^*$ Upper (mm)
S220503	226	531.81	754.72	1.42	67.19	43.29	2.93	0.33	0.01	0.136	0.214

Yin [32] also conducted similar research on S30408 duplex stainless steel under VGM, SMCS, and CVGM (Table 2). Zhang [37] also conducted similar research.

**Table 2.** Micromechanical model parameters. Reprinted with permission from Ref. [32]. 2019, Elsevier.

Steel	$E_0$ GPa	$\sigma_y$ MPa	$\sigma_u$ MPa	$\frac{\sigma_u}{\sigma_y}$	Z/%	A/%	$\eta$	$\lambda_{CVGM}$	$l^*$ Lower (mm)	$l^*$ Mean (mm)	$l^*$ Upper (mm)
S30408	249	273.85	710.38	2.59	76.02	62.35	3.314	0.29	0.01	0.220	0.780

### 3.4. Cyclic Void Growth Model (CVGM)

The VGM only covers the ductile fracture of metals under monotonic loading and neglects the ULCF problem caused by cyclic loading. Fracture morphology analysis reveals that ductile fracture characteristics are weakened under cyclic loads, making pure ductile fracture theory unsuitable for predicting ULCF problems. As a result, researchers have proposed cyclic void growth models based on this observation.

Kanvinde et al. [38–40] considered the influence of tensile and compressive cycles on void growth and proposed a cyclic void growth model (CVGM). In the CVGM, the void radius during cyclic loading can be expressed by the following Equation (17):

$$\ln(R/R_0)_{cyclic} = \sum_{tensile\ cycles} C_1 \int_{\epsilon_1}^{\epsilon_2} \exp(|1.5T|) d\epsilon_p - \sum_{compressive\ cycles} C_2 \int_{\epsilon_1}^{\epsilon_2} \exp(|1.5T|) d\epsilon_p \tag{17}$$

where  $T > 0$  is the tensile cycle, and  $T < 0$  is the compressive cycle; the first term on the right side of the equation represents the sum of the void growth at positive triaxiality,

and the second term represents the amount of void contraction due to plastic strain at negative triaxiality;  $C_1$  and  $C_2$  represent the growth rate and contraction rate of plastic strain, respectively. Assuming  $C_1 = C_2$ , the equation can be simplified as Equation (18):

$$\ln(R/R_0)_{cyclic} = C \left( \sum_{tensile\ cycles} \int_{\epsilon_1}^{\epsilon_2} \exp(|1.5T|) d\epsilon_P - \sum_{compressive\ cycles} \int_{\epsilon_1}^{\epsilon_2} \exp(|1.5T|) d\epsilon_P \right) \quad (18)$$

According to the void growth exponent formula in VGM, the void growth index under cyclic loading is Equation (19):

$$\ln(R/R_0)_{cyclic} = \sum_{tensile\ cycles} \int_{\epsilon_1}^{\epsilon_2} \exp(|1.5T|) d\epsilon_P - \sum_{compressive\ cycles} \int_{\epsilon_1}^{\epsilon_2} \exp(|1.5T|) d\epsilon_P \quad (19)$$

In the context of ULCF loading, the fracture process of the material involves the formation, growth, and coalescence of voids. The CVGM captures this fracture mechanism by modeling changes in plastic strain and triaxial stress. The life-triaxial stress relationships have been simulated using specimens with different notch radii. The results indicate that the material can withstand a greater number of cycles at larger notch radii, and the computational results were satisfactory. Compared to the previous VGM model, the CVGM results are more convincing. However, at the time the model was proposed, there was no explanation as to whether it could be applied to other scenarios, such as welded metals and large components. Further research is therefore required to determine the scope of its application in these contexts.

Song [41] used the CVGM to predict the ULCF life of corroded steel bridge piers. By analyzing parameters for different corrosion morphologies, it was revealed that fatigue cracks are typically initiated at the corner of fillet welds. Therefore, designers should aim to minimize the presence of sharp corners. In a similar study, Wang et al. [42] utilized an Abaqus subroutine based on the CVGM to investigate the damage process of steel frame beam-column joints under ULCF loading.

To improve the prediction accuracy of the CVGM, Adasooriya et al. [43] proposed a simple method for predicting the failure of steel structures under the interaction of fracture and fatigue based on the CVGM, with the criterion being Equation (20):

$$(\bar{\epsilon}_P^{cyclic})_{critical} = (\bar{\epsilon}_P^{monotonic})_{critical} \exp(-\lambda \bar{\epsilon}_P^{accumulated}) \quad (20)$$

$$\bar{\epsilon}_P^{cyclic} > (\bar{\epsilon}_P^{cyclic})_{critical} \quad (21)$$

When the cyclic plastic strain exceeds its critical value (Equation (21)), the material undergoes fracture behavior. Compared to the original CVGM, this model is easier to obtain initial model parameters that satisfy the fracture criterion. However, there are limitations to the simplified model, as it only applies to models where the triaxial stress remains constant during the loading process. The primary advantage of this approach is that the characteristic parameters of the hardening model are few, and the approach is simple.

Qiu [44] notes that current research lacks a systematic analysis of the ULCF performance of high-strength steel T-joints. Therefore, the Chaboche mixed hardening material parameters and fracture toughness parameters of the CVGM fracture prediction model were calibrated for various Q460 steel T-joints.

### 3.5. Degraded Significant Plastic Strain (DSPS) Model

Based on CVGM, the DSPS model [45] was obtained by considering the stress triaxiality as a constant in cyclic loading, and its micro-mechanical fracture criterion is Equation (22):

$$\epsilon_{eq}^P = \epsilon_t - \epsilon_c > (\epsilon_{eq}^P)_{critical} \quad (22)$$

$$(\epsilon_{eq}^p)_{critical} = \exp(-\lambda_{DSPS}\epsilon_p) \cdot \epsilon_p^{critical} \tag{23}$$

Similar to SMCS, parameter calibration for DSPS is relatively simple, but it only applies to situations where stress triaxiality does not significantly change. Liao et al. [46] calibrated the parameters of commonly used Q345 steel based on micro-mechanical fracture models, including the parameters of the monotonic models SMCS and VGM, as well as the parameters of the cyclic models DSPS and CVGM. After calibration, the micro-mechanical models SMCS, VGM, DSPS, and CVGM can be used to predict the fracture initiation of Q345 steel welding joints under both monotonic and cyclic loadings, respectively.

Yin et al. [47] calibrated the ULCF load of cast G20Mn5QT steel based on CVGM and DSPS (Table 3). They tested double-notch plate specimens of the cast steel under various loads to verify the accuracy of the two models.

**Table 3.** The model parameter calibration results for G20Mn5QT. Reprinted with permission from Ref. [47]. 2020, Elsevier Ltd.

Steel	E (GPa)	$\sigma_y$ (MPa)	$\sigma_u$ (MPa)	$\frac{\sigma_u}{\sigma_y}$	$\alpha$	$\eta$	$\lambda_{DSPS}$	$\lambda_{CVGM}$	$l^*$ Lower (mm)	$l^*$ Mean (mm)	$l^*$ Upper (mm)
G20Mn5QT	214	427	582	1.36	1.05	0.99	0.49	0.41	-	0.202	-

### 3.6. The Micromechanical Cyclic Void Growth Model (MM-CVGM)

Kiran et al. [29] investigated the influence of stress triaxiality and load parameters on void growth using the CVGM and proposed the MM-CVGM model to predict the ultra-low cycle life of ASTM A992 steel, with the damage formula expressed as Equation (24):

$$D = \sum_{T_\sigma^+} \int a_1 |T_\sigma|^{b_1} d\epsilon_m^p - \sum_{T_\sigma^-} \int a_2 |T_\sigma|^{b_2} d\epsilon_m^p \tag{24}$$

where  $a_1 = 5.45$ ,  $b_1 = 1.98$ ,  $a_2 = 4.52$  and  $b_2 = 1.93$ .

In Kiran et al.'s [28] study, a computational unit with an embedded spherical void was used to represent the microstructure of ASTM A992 steel in finite element analysis, assuming an initial void volume fraction of 0.01. Reduced integration and hourglass control were employed for discretized calculations [48], and the loading regime was cyclic loading. The results were fitted with experimental data, demonstrating the effectiveness of the MM-CVGM model in predicting the material's ultra-low cycle life. However, the model has limitations, such as only applying to high triaxial stress states and not considering the influence of the load parameter. Additionally, some of the conclusions in the article were verified under certain parameter assumptions. Therefore, further investigation is needed to explore the applicability of this model in other scenarios.

### 3.7. Lode Parameter Cyclic Void Growth Model (LCVGM)

In the ULCF prediction model mentioned earlier, the effect of triaxial stress and the load parameter on void growth was not taken into account. However, Huang et al. [49] considered the influence of shear stress, introduced the lode parameter, and proposed an enhanced cyclic void growth model (LCVGM) that takes into account shear effects. The model is expressed as Equation (25):

$$\begin{aligned} I_{CVG} &= \sum_{tensile} \int_{\epsilon_1}^{\epsilon_2} \exp(1.5|T|) \frac{1}{\beta+(1-\beta)\theta^{-2}} d\epsilon^{-P} \\ &- \sum_{compressive} \int_{\epsilon_1}^{\epsilon_2} \exp(1.5|T|) \frac{1}{\beta+(1-\beta)\theta^{-2}} d\epsilon^{-P} \\ &= \eta_M \exp(-\lambda \epsilon_{com}^{-P}) \end{aligned} \tag{25}$$

The load parameter range is denoted by the LCVGM equation above, while  $\bar{\theta} = 1$  represents the axisymmetric stress state. In this case, the LCVGM can be simplified to the CVGM, allowing the parameters calibrated with notched round bars for the CVGM to be accurately applied to the LCVGM.

The LCVGM parameters for the base metal and weld metal were determined based on experimental results from pure shear specimens. The ULCF fracture behavior of SHS bars in an X-joint with CHS supports was experimentally tested and simulated. Comparing the validation results of LCVGM and CVGM, it was found that CVGM often overestimates the actual ULCF life of the model. The proposed LCVGM, which considers the shear effect, accurately and consistently predicts the ULCF fracture mode of the X-joint in line with experimental results. Figure 12 depicts a schematic diagram of the experimental loading setup.

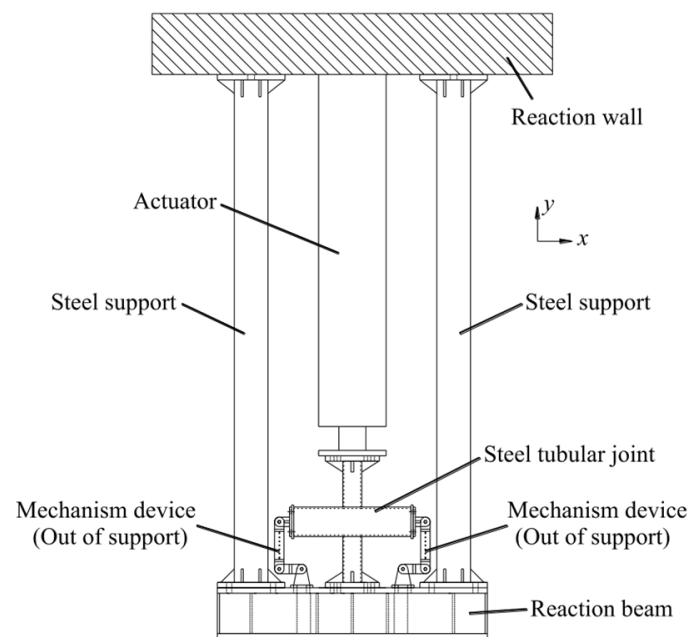


**Figure 12.** Loading sketch of X-joint with SHS chord to CHS braces. Reprinted with permission from Ref. [49]. 2021, Elsevier.

### 3.8. Improved Cyclic Void Growth Model (ICVGM)

Li et al. [50] proposed an improved model, ICVGM, which is a combination of the CVGM and DSPS models. The ICVGM takes into account the relationship between the cyclic damage degradation parameter and the stress triaxiality. To establish this relationship, an empirical formula is employed, linking the cyclic damage degradation parameter to the stress triaxiality as expressed in Equation (26):

$$\begin{cases} \lambda_{CVGM} = f(\bar{T}) \\ \lambda_{DSPS} = g(\bar{T}) \end{cases} \quad (26)$$

where  $T(\varepsilon_p)$  denotes the loading history of stress triaxiality. The specific function forms of  $f(\bar{T})$  and  $g(\bar{T})$  are determined by the subsequent parameter calibration. To validate the prediction accuracy of the newly proposed ICVGM model, triaxial stresses ranging from 0.45 to 0.9 were employed. The original model parameters were also calibrated, and the difference between the experimentally observed crack initiation and the predicted model was compared. The results showed that the accuracy of the ICVGM model, which takes into account the dependence of cyclic damage parameters on triaxial stress, is higher than that of the original model.

In subsequent studies, to address the issue of high prediction costs caused by a large number of model parameters, Li et al. [51] proposed a single-parameter model to predict the

ULCF damage of structural steel based on the concepts of ductile damage under monotonic tension and cyclic damage under cyclic loading. The model parameters were calibrated under monotonic tension. The ductile damage under tensile load can be expressed as shown in Equation (27):

$$D_{\text{ductile}} = \int_0^{\varepsilon_c} \frac{1}{\varepsilon_f(T)} d\varepsilon_{eq}^p \quad (27)$$

The cyclic damage under cyclic loading can be evaluated using the following damage index as Equation (28):

$$D_{\text{cyclic}} = \begin{cases} \int_0^{\varepsilon_c} \left( \frac{\varepsilon_{pt}}{\varepsilon_f(T)} \right) \frac{d\varepsilon_{eq}^p}{\varepsilon_f(T)} & T \geq -1/3 \\ 0 & T < -1/3 \end{cases} \quad (28)$$

In this study, no damage accumulates when stress triaxiality is below  $\frac{1}{3}$ . In Equation (29):

$$\varepsilon_f(T) = \ln \frac{R_f}{R_0} / (C \cdot \exp(1.5T)) = \alpha \cdot \exp(-1.5T) \quad (29)$$

The ductile fracture of material occurs when plastic strain reaches plastic fracture strain. The expression for the new damage model is Equation (30):

$$D_{ULCF} = D_{\text{ductile}} + D_{\text{cyclic}} \quad (30)$$

During the deduction process, the only unknown in the model is the  $\alpha$  material parameter that determines the critical plastic fracture strain. When the plastic strain reaches the plastic fracture strain, the material undergoes ductile fracture.

### 3.9. The Summary of This Section

The proposed prediction model offers theoretical support for predicting the life of materials under cyclic loading. However, material void growth theory is a complex process, and it may be challenging to obtain practical results solely relying on theoretical models. Therefore, when developing theoretical models, it is essential to pay more attention to the consistency between theory and practice. In Table 4, a summary of the life prediction models for this section is provided.

**Table 4.** Microcosmic ductility fracture model based on void growth.

No.	Name	Material	Loading Protocol	Reference
1	Coffin-Manson model	Aluminum alloy 7075-T6	C-PTF CTF	[15,16]
2	XUE Model	2024-T351 aluminum alloy	CTF	[21,22]
3	VGM	SS400 steel (BRB)	Monotonic loading	[24]
4	MM-VGM	ASTM A992 Steel	Monotonic loading	[28]
5	SMCS	Three rolled, low alloy, quenched, and tempered sheets of steel AS72-Grade 50 A572-Grade 50 AS14-Grade 110	Monotonic loading	[30]
6	CVGM	HPS70W JIS-SN490B Grade 50 JIS-SM490YBTMC-5L Grade 50 JIS-SN490B Grade 50	C-PTF CTF	[38–40]

Table 4. Cont.

No.	Name	Material	Loading Protocol	Reference
7	DSPS	AS72-Grade 50	C-PTF CTF	[45]
		A572-Grade 50		
		AS14-Grade 110		
		HPS70W		
		JIS-SN490B Grade 50		
8	MM-CVGM	JIS-SM490YBTMC-5L Grade 50	CTF	[29]
		JIS-SN490B Grade 50		
9	L-CVGM	ASTM A992 steel	CTF	[49]
10	ICVGM	Q345qC	C-PTF	[50]
			CTF	

CTF = cycle to failure. The specimen is cycled between the displacement limits (in mm) described in the parentheses. C-PTF = cycle and pull to failure. The specimen is cycled between displacement limits (or a series of displacement limits) and then pulled in tension to failure.

#### 4. Fracture Model Based on Porous Plasticity

##### 4.1. Gurson-Tvergaard-Needleman (GTN) Model

Gurson et al. [52] were the first to propose a yield function constitutive model for ductile metals based on material spherical voids. This model considers the influence of hydrostatic pressure, void volume fraction, and equivalent stress on the yield function, and couples material plasticity and ductile fracture. Rudnicki [53] and Yamamoto [54] considered local shear factors and obtained optimized models. Subsequently, Tvergaard [55–57] and Needleman et al. [58] modified the Gurson model parameters, and the new model is called the Gurson-Tvergaard-Needleman (GTN) model, which is widely used in predicting the failure analysis of metal materials. The expression for the yielding function is as follows [59]:

$$\phi = \frac{3\sigma'_{ij}\sigma'_{ij}}{2\sigma^2} + 2q_1f^* \cosh\left(\frac{3\sigma_m}{2\sigma}\right) - [1 + (q_1f^*)^2] = 0 \quad (31)$$

$$f^* = \begin{cases} f & \text{for } f \leq f_c \\ f_c + K(f - f_c) & \text{for } f > f_c \end{cases} \quad (32)$$

where  $f_c$  is the critical value at which void coalescence occurs. The parameter defines the slope of the sudden drop of the load on the load-diameter reduction diagram and is often referred to as the accelerating factor. For  $f^* = 0$ , the plastic potential (Equation (32)) is identical to that of Von Mises.

##### 4.2. The Application and Development of the GNT Model

The GNT model optimized by Mear et al. [60] can not only predict uniaxial loading but also cyclic loading by considering isotropy and kinematic hardening. Leblond et al. [61] introduced kinematic hardening into porous plasticity and proposed the GTN-LPD (Leblond, Perrin, and Devaux) model.

Huang et al. [62] conducted a study on beam-column welded joints (Figure 13) and used the GNT model to verify the prediction of node-bearing capacity and fracture load under both monotonic and cyclic loading conditions. The displacement-load curves for both the experiment and simulation shown in Figure 14 exhibit consistent trends, indicating agreement between the results. The study involved calibrating the hardening model parameters and micro-mechanical damage model parameters for the base metal, weld metal, and welding zone of a Q345 beam-column welded joint through monotonic stretching experiments (as shown in Table 5). Based on the experimental data, simulation analysis was conducted, and the results were found to be highly consistent with previous experimental findings. This confirms the reliability of the micro-mechanical damage model for predicting the fatigue life of beam-column welded joints under both cyclic and monotonic loading.

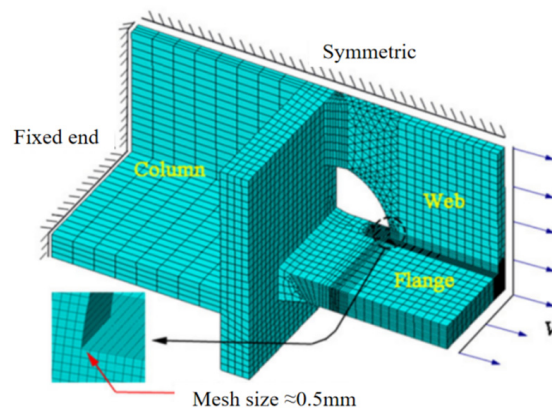


**Figure 13.** Finite element mesh of beam-column welded joints. Reprinted with permission from Ref. [62]. 2013, Elsevier.

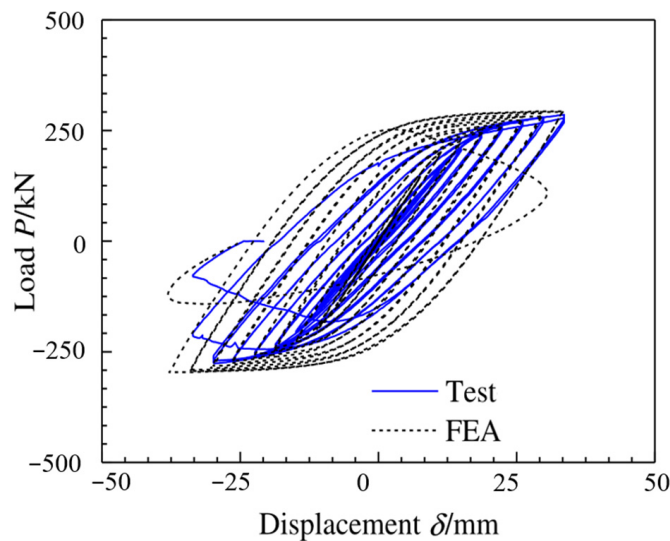


**Figure 14.** Comparison of FEA with test results for load versus displacement relations of welded joints. Reprinted with permission from Ref. [62]. 2013, Elsevier.

**Table 5.** Parameters of micromechanics damage constitutive model. Reprinted with permission from Ref. [62]. 2013, Elsevier.

$\sigma_0$ /MPa	$\sigma_m$ /MPa	$b$	$C_1$ /MPa	$b_1$	$C_2$ /MPa	$b_2$	$f_0$	$f_c$	$f_F$	$f_N$	$\epsilon_N$	$s_N$	$q_1$	$q_2$
346	150	8	7000	80	660	0.8	0.0050	0.25	0.28	0.04	0.3	0.1	1.5	0.71
402				300			0.0100							
366				110			0.0085							

Wang et al. [63] calibrated the initial parameters of Q690 high-strength steel and welded joints based on the GTN model using an exhaustive search method and particle swarm algorithm and achieved good simulation results. Oh [64] simulated the ductile fracture process of STPT410 carbon steel pipes under pure bending using the GTN model and incorporated the size effect of finite elements into the GTN model. The study also considered the influence of crack tip mesh design on determining GTN model parameters. Li [65] qualitatively described the influence of element size on damage parameters for DP600 cold-rolled high-strength steel plates under different stress conditions, based on the GTN damage model incorporating strain gradient plasticity and shear correction, combined with experimental and simulation results. Qiang et al. [66] calibrated the parameters of the GTN model (as shown in Table 6) through uniaxial tensile and single-edge notched bending tests on X80 pipeline base metal, weld metal, and heat-affected zone. The calibrated GTN

model was then used to analyze the behavior of ductile crack propagation in single-edge notched tension tests at different locations of the weld.

**Table 6.** GTN model parameters and  $N$  for different X80 weld joint locations. Reprinted with permission from Ref. [66]. 2019, Elsevier.

Locations	$q_1$	$q_2$	$q_3$	$\epsilon_N$	$S_N$	$f_0$	$f_c$	$f_F$	$f_N$	$N$
WM	1.5	1	2.25	0.3	0.1	0.001	0.2	0.2	$1.54 \times 10^4$	0.06
CGHAZ	1.5	1	2.25	0.3	0.1	0.0006	0.2	0.2	$4.77 \times 10^5$	0.11
FGHAZ	1.5	1	2.25	0.3	0.1	0.002	0.2	0.2	$4.77 \times 10^5$	0.10
ICHAZ	1.5	1	2.25	0.3	0.1	0.0025	0.2	0.2	$4.77 \times 10^5$	0.09
BM	1.5	1	2.25	0.3	0.1	0.00025	0.2	0.2	$4.77 \times 10^5$	0.06

#### 4.3. The Summary of This Section

The GTN model can characterize the nucleation, growth, and merging of voids, but this model has more than 10 parameters to determine a single material, which is difficult in practical applications [67,68]. Coupled models are more reasonable considering the material degradation caused by pore growth and agglomeration, which can more accurately predict the ductile fracture of materials [69]. However, considering the complexity of the coupled micromechanical fracture model, non-coupled micromechanical fracture models are still the basic models that provide simple and convenient guidelines for predicting ductile fracture in engineering practice [70].

### 5. Fracture Model Based on Micromechanical Damage

Fracture models at the fine level of the material target scales in the range of  $10^{-2}$ – $10^{-1}$  mm, while the scales for metals are in the range of  $10^2$ – $10^3$  mm. Continuous damage mechanics provides an alternative approach to modeling ductile fractures at the macroscopic level. In 1958, Kachanov first proposed the macroscopic damage index for predicting creep fracture [71]. Later, Chaboche [72] and Lemaitre [73] established constitutive models of continuum damage mechanics within the framework of thermodynamics.

#### 5.1. Barcelona Plastic Damage Model

The Barcelona plastic damage model, proposed by Lubliner et al. [74] in 1989, is a damage model based on the principle of energy dissipation. It can be used to predict the ULCF of concrete under irregular cyclic loading. The influence of elastic-plastic stiffness degradation was considered. By simple post-processing of the finite element model, the starting time and quantity of cracks can be obtained, and the effectiveness of the model can be validated. However, the model was originally proposed for concrete materials, and further verification is needed to predict the ULCF life of structural steel.

Martinez et al. [75] proposed the use of the Barcelona damage model and a specially designed isotropic hardening law to simulate steel and analyze ULCF problems, predicting the material's life by considering the fracture energy dissipation of the material. The model assumes that damage begins when the plastic law reaches the softening zone, and the material completely fails when all the fracture energy is dissipated. Another advantage of this model is its considerable prediction accuracy for irregular cyclic loading. Figure 15 shows Response of the model after ten seismic-type cycles.

Further verification is required to determine whether the Barcelona model has a significant predictive effect in practical engineering applications. Due to the complexity of the theory and the parameters of the model, its application in predicting ULCF life is not common in subsequent research.

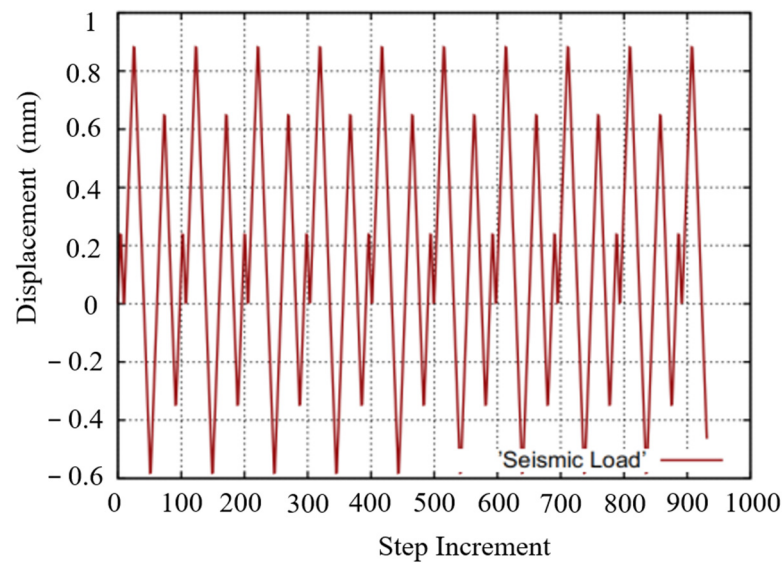


**Figure 15.** Response of the model after ten seismic-type cycles. Reprinted with permission from Ref. [75]. 2015, Elsevier.

### 5.2. The Damage Model Based on CVGM

The researchers utilized the void growth process in CVGM to represent the accumulation of damage. By integrating the void growth index with the concept of damage, a crack initiation criterion was obtained that better reflects engineering reality. The degree of material damage can be used to better reflect the level of fatigue.

Li et al. [76] proposed a model parameter calibration method that separately calibrated the damage degradation parameters under high-stress triaxiality and medium-stress triaxiality, as shown in Equation (33):

$$VGI_{cyclic}^{crit} = VGI_{mon}^{crit} \exp(-\lambda \epsilon_p^{accu}) \quad (33)$$

$$f = VGI_{cyclic}^{crit} / VGI_{mon}^{crit} = \exp(-\lambda \epsilon_p^{accu}) \quad (34)$$

where  $f$  is the material damage rate. When  $VGI_{cyclic}^{crit}$  exceeds  $VGI_{cyclic}$ , the material undergoes ultra-low-period fatigue damage. To quantify the degree of damage from ultra-low-period fatigue, the damage index is defined as Equation (35):

$$\begin{cases} D = \max\{D_{n-1}, D_{th}\} \\ D_{th} = 1 - \frac{(VGI_{cyclic}^{crit} - VGI_{cyclic})}{VGI_{mon}^{crit}} \end{cases} \quad (35)$$

During the loading process, if  $D_{th}$  exceeds the previous step, it is updated  $D_{th}$ , otherwise, it remains unchanged. When  $D$  reaches 1, it is considered that ULCF has occurred. The parameter calibration method proposed by this model reduces the randomness of experimental results and the range of triaxial stress. The curve shown in Figure 16 represents the cumulative process of damage during cyclic loading. The increasing part of the curve represents the damage caused by the growth of voids due to loading, while the horizontal part of the curve represents the unloading process during the latter half of the cycle, with zero damage. The figure presents the results of two different specimens with different notch radii: Figure 16a,c have a notch radius of 7.5 mm, while Figure 16b,d have a notch radius of 15 mm. The different radii represent distinct levels of triaxial stress.

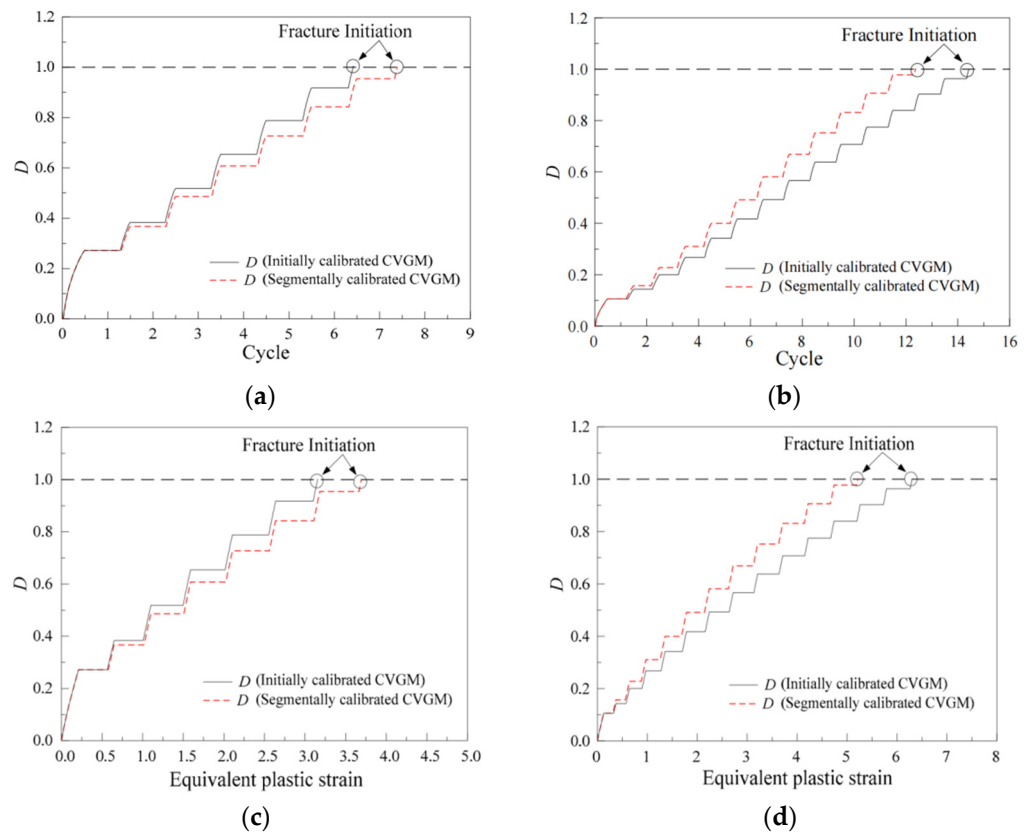


**Figure 16.** Evolution of the damage index: (a) cumulative damage  $R = 7.5$  mm; (b) Damage and Equivalent Plastic Strain Curve  $R = 7.5$  mm; (c) cumulative damage  $R = 15$  mm; (d) Damage and Equivalent Plastic Strain Curve  $R = 15$  mm. Reprinted from Ref. [76].

Xiang et al. [77] proposed a new ULCF model based on the CVGM that highlights how the model may underestimate the number of cycles to failure. The authors divided metal hardening into isotropic hardening (IH) and kinematic hardening (KH). Figure 17 shows the stress triaxiality and equivalent plastic strain curves, with the IH and KH strain increments decomposed for positive and negative stress triaxialities. Under the same plastic strain conditions, IH often causes more damage than KH. Assuming that IH and KH have different damage accumulation rates in the same stage, the expression for the damage increment is given by Equation (36):

$$dD_{ULCF} = dD_{IH} + dD_{KH} \tag{36}$$

Assuming the CVGM damage accumulation rule holds, i.e.,

$$dD_{IH} = \begin{cases} \frac{d\epsilon_{eq}^p}{\chi_{cr} \cdot e^{-1.5T}}, T \geq -\frac{1}{3} \\ 0, T < -\frac{1}{3} \end{cases} \tag{37}$$

And have a linear relationship:

$$dD_{KH} = \begin{cases} \eta_c \frac{d\epsilon_{eq}^p}{\chi_{cr} \cdot e^{-1.5T}}, T \geq -\frac{1}{3} \\ 0, T < -\frac{1}{3} \end{cases} \tag{38}$$

The numerical values of the two damage indicators and the equivalent plastic strain curve are shown in Figure 18. The slope of the curve is the same at the beginning of the first and third half cycles. According to the definition in Figure 17, the damage is related

to IH damage. The curve also includes many flat plateaus, which correspond to the stress state at  $T = -1/3$ . When the damage accumulates to 1, the material undergoes a fracture.

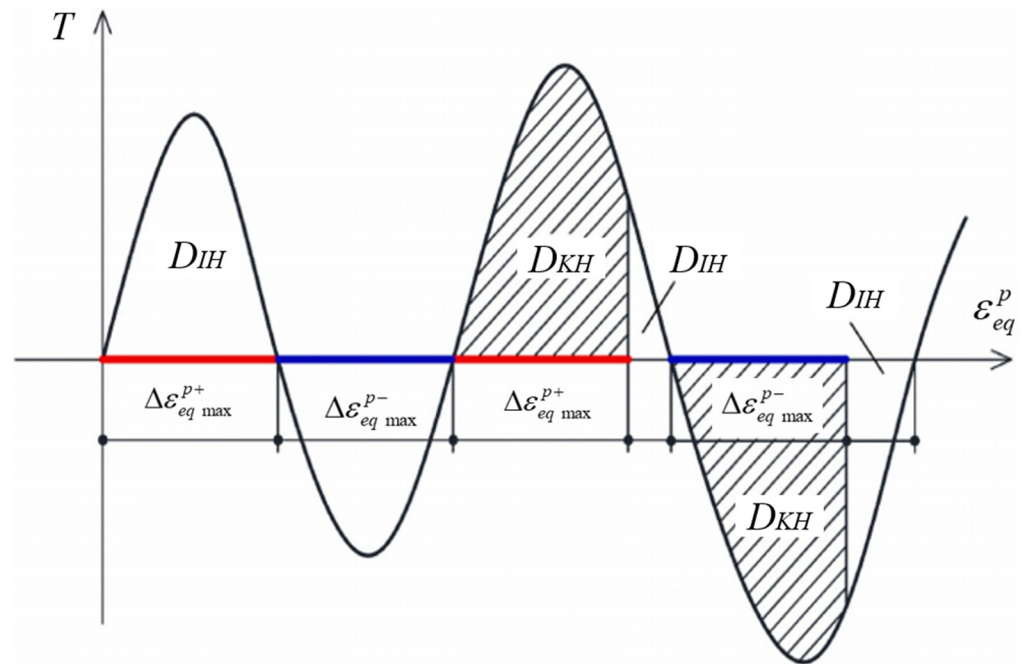


**Figure 17.** Decomposition of isotropic and kinematic hardening-correlated damage. Reprinted with permission from Ref. [77]. 2020, Elsevier.

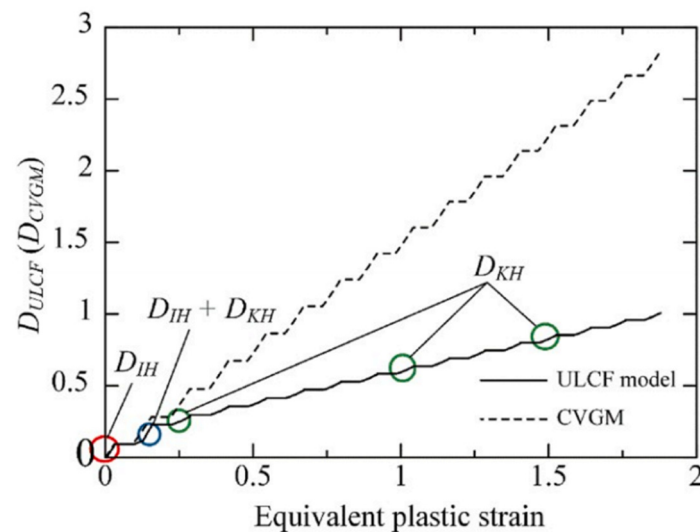


**Figure 18.** Damage accumulation histories for different fracture models. Reprinted with permission from Ref. [77]. 2020, Elsevier.

### 5.3. Continuous Damage Model (CDM)

The CDM is a method for predicting damage using the ULCF approach. By introducing a damage variable, this model can directly describe the macroscopic mechanical behavior and damage evolution process of materials [78]. The expression for CDM in the ULCF direction is Equations (39) and (40):

$$dD = \alpha \frac{(D_{cr} - D_0)^{1/\alpha}}{\ln(\varepsilon_f / \varepsilon_{th})} f\left(\frac{\sigma_m}{\sigma_{eq}}\right) (D_{cr} - D)^{(\alpha-1)\alpha} \frac{d\varepsilon^{p+}}{\varepsilon^p} \quad (39)$$

$$\begin{cases} d\varepsilon^{p+} = d\varepsilon^p \cdot H(T) \\ H(T) = \begin{cases} 0 & T < 0 \\ 1 & T \geq 0 \end{cases} \end{cases} \quad (40)$$

The damage modulus of the material for Equation (41) is as follows:

$$E = E_0[1 - D \cdot H(T)] \quad (41)$$

The researchers calibrated the parameters through monotonic tensile tests by using the deformation corresponding to the sudden drop point of the displacement-load curve as the monotonic plastic strain threshold (as shown in Figure 19). In finite element analysis, the stress triaxiality  $T$  and accumulated plastic strain at the notch bottom were recorded and used to calibrate the model through Equation (37) when the elongation length of the extensometer reached the experimental plastic strain threshold.

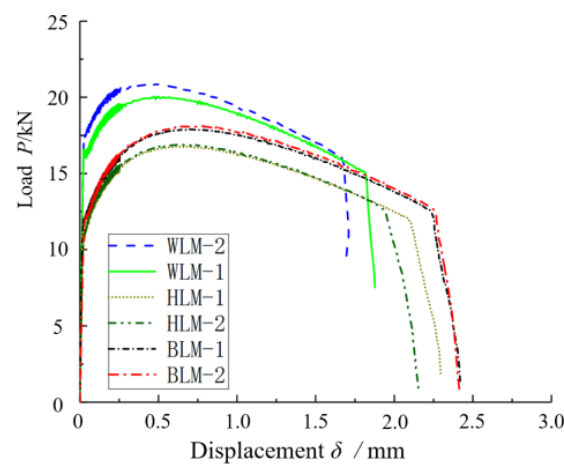


**Figure 19.** Load-deformation curves of notched round bar specimens at the gauge segment with notch radii. Reprinted from Ref. [78].

This method is not only suitable for analyzing toughness, but also for modeling brittle fracture damage behavior [79]. Compared to CVGM, the CDM model is capable of predicting the relationship between fatigue and fatigue life, fracture life, the post-fracture path, and the number of cycles for initial damage. Additionally, the parameter calibration for the CDM model is simple, and the prediction error is small. The finite element size is not limited by the characteristic length, making the calculation efficiency high [80]. Furthermore, the CDM model can represent the evolution law of damage and the post-fracture path [81].

#### 5.4. Stress-Weighted Ductile Fracture Model (SWDFM)

The SWDFM [82,83] is expressed as follows:

$$D = \int dD = C_{SWDFM} \times \int_0^{\varepsilon_p} [2 \times \exp(1.3T) - \exp(-1.3T)] \cdot \exp[k_{SWDFM}(|X| - 1)] \cdot d\varepsilon_p \geq 1 \quad (42)$$

Zhu et al. [84] applied the stress-weighted ductile fracture model (SWDFM) to predict ULCF fracture of buckling steel brackets and investigated the effectiveness of the model in predicting fracture of large structural components. The experimental results were compared with the model predictions, and the results are shown in Figure 20. The fracture point is indicated by the star-marker in Figure 20, as per Equation (42).

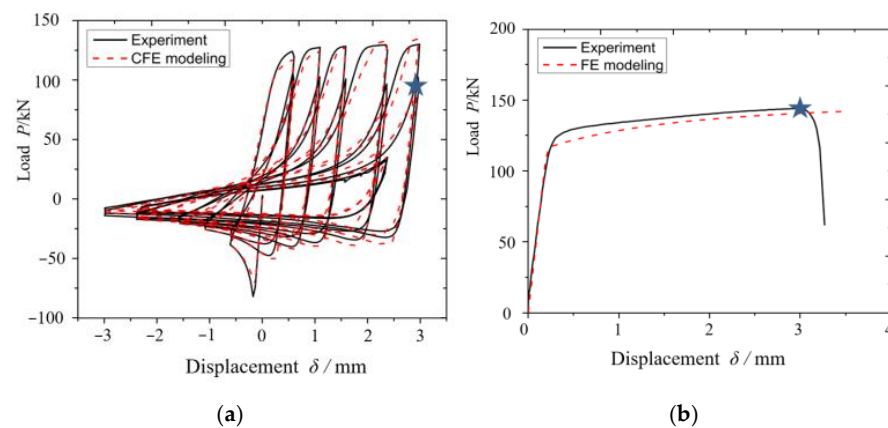


**Figure 20.** Force-deformation comparisons between experiments and ABAQUS simulations for the Pipe3STD brace (a) cyclic loading, (b) monotonic test. Reprinted with permission from Ref. [84]. 2021, Elsevier.

Di et al. [85] proposed a continuous medium damage mechanics model, Equation (43):

$$d_{inc} = \begin{cases} d_f \cdot \sqrt{\|\frac{2}{3}\epsilon^p\| - d_p}, & T \geq 0 \\ 0, & T < 0 \end{cases} \quad (43)$$

The model considers the influence of reverse loading on damage and applies the concept of effective strain to only calculate the cumulative damage during the tensile stage.

### 5.5. Liu Model [86]

Liu proposed formulas for predicting crack initiation based on the ductility ratio and equivalent plastic strain. The definition of ductility ratio is Equation (44):

$$\mu_{pi} = \frac{|\delta_i - \frac{P_i}{K_e}|}{\delta_{y0}} \quad (44)$$

According to the Mason-Coffin rule, the crack initiation life (loading half cycles  $N_{fi}$ ) can be expressed in terms of the ductility ratio in Equation (45) as follows:

$$N_{fi} = C_d \cdot (\mu_{pi})^{k_d} \quad (45)$$

However, Equation (37) applies to cases under constant loading amplitudes. To apply to the ones under random loading amplitudes, a damage index  $D$  can be defined according to the linear damage accumulation rule, i.e., Miner’s rule, as Equation (46):

$$\Delta D_i = \frac{1}{N_{fi}} \quad (46)$$

where  $\Delta D_i$  is the incremental damage during the  $i$  – th loading half cycle. Failure is postulated to occur when  $D$  reaches 1.

Previous methods for evaluating ULCF were based on the plastic strain method of the material, which resulted in high calculation costs. To address this issue, Xie et al. [87] proposed a new damage index based on the deformation process of the material. For structures with a variable deformation amplitude, the cumulative damage index  $D$  is calculated using Equation (47):

$$D = \sum_{i=1}^n \frac{1}{N_{f,i}} = \frac{1}{2k_1} \sum_{i=1}^n (\Delta\delta_i)^{-k_2} \quad (47)$$

The cumulative damage index  $D$  is equal to zero when there is no damage, and it is assumed that structural failure would occur if  $D = 1$  is satisfied.

### 5.6. Cyclic Multiaxial Fracture Strain Energy (CMFSE)

The CMFSE model was developed based on the Multi-Axial Fatigue Strain Energy (MFSE) model with the stress correction proposed by Nam. In [88], to account for the expansion and contraction of micro-voids during cyclic loading, the accumulated effective equivalent plastic strain energy is defined using Equation (48):

$$W_{p,cyc}^{eff} = \sum sign(T) \Delta W_{p,cyc} = \sum sign(T) (\sigma - \alpha) : \Delta \varepsilon_{pl} \quad (48)$$

The signed term operates as a sign  $(T) = 1$  when  $T \geq 0$  and sign  $(T) = -1$  when  $T < 0$ . The  $\varepsilon_{pl}$  denotes the plastic strain tensor,  $\sigma$  and denotes the stress tensor and back stress tensor.

### 5.7. Cyclic Lode Parameter Enhanced Continuum Damage Mechanics (CLCDM) Model

In [13], the author proposed a new damage-based life prediction model, the expression of which is given in Equation (49):

$$dD = \alpha \frac{(D_{cr} - D_0)^{1/\alpha}}{\ln(\varepsilon_f / \varepsilon_{th})} f\left(\frac{\sigma_m}{\sigma_e}\right) (D_{cr} - D)^{1-1/\alpha} \frac{1}{\beta + (1 - \beta)\bar{\theta}^2} \frac{d\bar{\varepsilon}_c^{p+}}{\bar{\varepsilon}^p} \quad (49)$$

### 5.8. The Summary of this Section

In Table 7, a summary of the life prediction models for this section is provided.

**Table 7.** Fracture model based on micromechanical damage.

No.	Name	Material/Application	Loading Protocol	Reference
1	Barcelona Plastic Damage Model	Concrete	Monotonic loading	[74]
2	Improve Barcelona Plastic Damage Model	X52 steel	ULCF loading	[75]
3	CDM	Q345qC	ULCF loading	[78]
4	Liu Model	welded T-joints	CTF	[86]
5	CMFSE	Mn-Si steel	C-PTF CTF	[88]
6	CLCDM	Q235 & Q690	Monotonic loading ULCF loading	[13]

## 6. Summary

In most cases, ULCF causes the extension of ductile cracks inside the steel, whose mechanism is very different from plain fatigue, ultimately leading to material failure. In recent years, a number of studies have been carried out by many research institutions to better understand this degradation mechanism. Research has focused on the accurate measurement of plastic strain, the development and validation of effective predictive models, and the study of the microstructural evolution of damage mechanisms.

From the current research results, the study of ultra-low circumference fatigue has made great progress in revealing the nature and mechanism of fatigue damage to structural materials. It has also provided important theoretical support for engineering practice. In this paper, ULCF life prediction models are classified into three types: microcosmic ductility fracture model based on void growth; fracture model based on porous plasticity; fracture model based on micromechanical damage. The development history of each type of model is shown in Figure 21. The conclusions are as follows:

- (1) VGM has the disadvantage of only describing void growth without providing a ductile fracture criterion. The cyclic void growth model (CVGM) extends the theory to cyclic loading and includes mechanisms such as void nucleation, void growth, void coalescence, and fracture. This is currently the recognized theory, and improvements have been made to the model to consider the effects of stress triaxiality and load parameters.
- (2) GNT shows higher prediction accuracy when void parameters are considered in the application process. However, the model has 10 unknown parameters, making parameter calibration difficult.
- (3) The models introduce damage as a criterion for material fracture, which is more in line with engineering reality. The degree of material damage can better reflect changes in fatigue life. The model has high prediction accuracy, and the accumulation process of damage can better reflect the internal fatigue condition of the material. However, multiple factors, such as stress state and load history, also need to be considered.

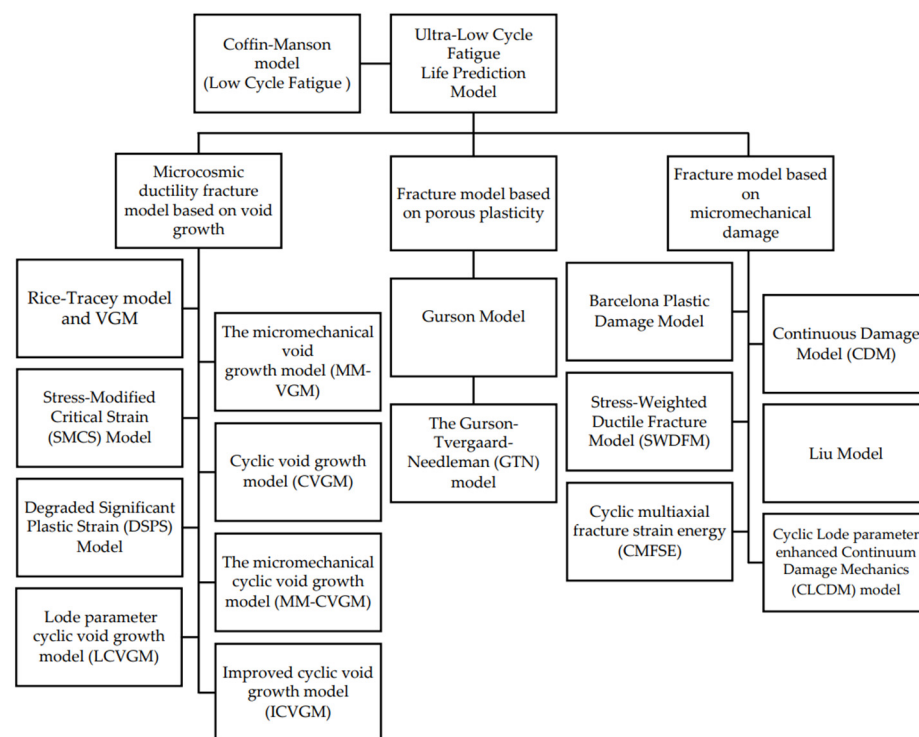


**Figure 21.** Classification of the ULCF life prediction model [14–16,24,26,28–30,38–40,45,49–52,55–58,74,78,80–83,86].

Future research priorities of the ULCF should include the improvement of measurement techniques and standards, the study of the fatigue failure mechanism and its microstructural evolution characteristics, and the discovery and development of more efficient and reliable material and structural design methods. ULCF research has made significant progress in understanding fatigue damage mechanisms and providing theoretical support for engineering practice. Future research should focus on improving measurement techniques and standards, investigating failure mechanisms and microstructure evolution characteristics, and developing more efficient material and structural design methods.

**Author Contributions:** Investigation, writing—original draft preparation: Y.X. and X.L.; writing—editing: Y.X.; writing—review: X.L.; visualization: X.L. and Y.Z.; supervision, management: Y.Z. and J.Y. All authors have read and agreed to the published version of the manuscript.

**Funding:** National Natural Science Foundation of China Youth Fund Project (51905028), Beijing Municipal Education Commission Science and Technology Plan General Project (KM202110016002), Beijing University of Civil Engineering and Architecture Pyramid Talent Training Project (JDYC20200323).

**Data Availability Statement:** Not applicable.

**Acknowledgments:** Thanks to the above funds.

**Conflicts of Interest:** The authors declare no conflict of interest.

## Nomenclature

$\Delta\varepsilon_p$	plastic strain range
$N_f$	number of half cycles to fail
$k$	material-dependent constants
$C$	material-dependent constants
$n_i$	the number of half cycles
$N_{fi}$	fatigue life in the $i$ th plastic strain range
$\Delta\varepsilon_{eq}$	multiaxial plastic strain range
$T$	stress triaxiality
$C(T), k(T)$	$C(T)$ and $k(T)$ are determined by the parameter calibration
$\varepsilon_d$	$\varepsilon_d = \sqrt{\frac{2}{3}} \sqrt{\varepsilon_1^2 + \varepsilon_2^2 + \varepsilon_3^2}$ ( $\varepsilon_1, \varepsilon_2, \varepsilon_3$ are the three principal components of the plastic strain tensor)
$\varepsilon_f$	fracture strain
$R$	cavity radius
$\varepsilon_{eq}$	equivalent strain
$d\varepsilon_{eq}^p$	equivalent plastic strain increment
$\varepsilon_{fr}(T)$	the functions related to the triaxiality of stress define the material properties
$d_{int}(\varepsilon_{eff}, T_\sigma)$	damage integral
$d_{cr}$	critical damage index
$l^*$	characteristic length
$\lambda_{c0}$	computational cell aspect ratio
$\lambda_{v0}$	void aspect ratio
$f_0$	initial void volume fraction
$f_R$	micromechanical void growth indicator
$T_\sigma$	macroscopic stress triaxiality
$l_{z0}$	initial length of the computational cell
$l_{r0}$	initial radius of the computational cell
$r_{r0}$	initial semi axial length of void in r-direction
$r_{z0}$	initial semi axial length of void in z-direction
$\Sigma_{rr}$	macroscopic stress in $r$ direction
$\Sigma_{zz}$	macroscopic stress in $z$ direction
$R_0$	initial void size
$\sigma_e$	effective stress
$\sigma_m$	actual yield stress of the matrix
$\varepsilon_p^{critical}$	critical value of cumulative equivalent plastic strain
$VGI_{critical}$	critical void growth index
$(\varepsilon_p^{cyclic})_{critical}$	critical value of cumulative equivalent plastic strain under cyclic loading
$(\varepsilon_p^{monotonic})_{critical}$	critical value of cumulative equivalent plastic strain under monotonic loading
$VGI_{cyclic}^{crit}$	void growth rate under monotonic loading
$E$	elasticity modulus
$\sigma_y$	yield stress
$\sigma_u$	tensile stress
$\eta$	toughness parameter
$\lambda_{CVGM}$	damage degraded parameter of the material under cyclic loading

$f$	material damage rate
$n$	number of incremental steps
$D_{th}$	damage index value calculated
$D$	total damage
$D_{IH}, D_{KH}$	the associated damage of IH and KH
$\varepsilon_m^p$	the macroscopic strain
$\beta$	It reflects the effect of the Lode parameter on the cyclic cavity growth index
$\theta$	range of values of the Load parameter
$\bar{T} = \frac{1}{\varepsilon_f} \int_0^{\varepsilon_f}  T(\varepsilon_p)  d\varepsilon_p$	average stress triaxiality
$\varepsilon_f$	plastic fracture strain
$\varepsilon_{pt}$	transient plastic strain
$\varepsilon_{ft}/\varepsilon_f(T)$	damage rate of material
$T(\varepsilon_p)$	loading history of stress triaxiality
$R_f$	critical void radius
$\sigma$	actual yield stress of the matrix of the material
$\sigma'_{ij}$	stress deviator
$f^*$	function of the void volume fraction
$f_c$	critical value at which void coalescence occurs
$f_N$	volume fraction of nucleated voids
$f_F$	maximum volume fraction of microvoids
$\varepsilon_N, s_N$	the mean equivalent plastic strain and standard deviation at void nucleation, respectively
$q_1, q_2, q_3$	damage correction factor for interaction between adjacent microvoids
$\varepsilon^{p+}$	plastic tensile strain
$H(T)$	damage state
$\lambda_{DSPS}$	material degradation parameter for DSPS model
$d_0$	initial diameter
$d_f$	final diameter
$C_d, k_d$	material constants
$\varepsilon_{pl}$	plastic strain tensor
$\varepsilon_{th}$	plastic strain threshold under uniaxial stress
$D_{cr}$	critical damage variable
$E_0$	elastic modulus before damage
$E$	elastic modulus after damage
$H(T)$	damage state
$C_{SWDFM}, k_{SWDFM}$	material constants
$d_{inc}$	Damage increment
$d_f$	Parameter for damage evolution
$\delta_i$	plastic displacement of the $i$ -th loading half cycle
$\delta_{y0}$	initial yield displacement of the first loading half cycle
$\Delta D_i$	incremental damage
$\Delta \delta_i$	constant amplitude loads of deformation range
$\Delta W_{p,cyc}$	incremental equivalent plastic strain energy
$W_{p,cyc}^{eff}$	accumulated effective equivalent plastic strain energy
$\sigma, \alpha$	stress tensor and back stress tensor, respectively
$\eta_c$	material constant

## References

1. Santagati, S.; Bolognini, D.; Nascimbene, R. Strain Life Analysis at Low-Cycle Fatigue on Concentrically Braced Steel Structures with RHS Shape Braces. *J. Earthq. Eng.* **2012**, *16*, 107–137. [[CrossRef](#)]
2. Nip, K.H.; Gardner, L.; Davies, C.M.; Elghazouli, A.Y. Extremely low cycle fatigue tests on structural carbon steel and stainless steel. *J. Constr. Steel Res.* **2010**, *66*, 96–110. [[CrossRef](#)]
3. Gong, S.; Sheng, G. Influence of the toughness of steel for earthquake-resistant buildings on the seismic performance of buildings. *Earthq. Resist. Eng.* **2004**, *01*, 41–47.
4. Pereira, J.C.R.; de Jesus, A.M.P.; Xavier, J.; Correia, J.A.F.O.; Susmele, L.; Fernandes, A.A. Low and ultra-low-cycle fatigue behavior of X52 piping steel based on theory of critical distances. *Int. J. Fatigue* **2020**, *134*, 105482–105489. [[CrossRef](#)]
5. Luo, Y.; Wang, Q.; Fu, L.; Zhang, Y.; Tao, J.; Xie, W. Ultra-low Cycle Fatigue Performance of Q235 Steel Structural Material. *J. Iron Steel Res.* **2016**, *28*, 47–51.

6. Pereira, J.C.R.; De Jesus, A.M.P.; Xavier, J.; Fernandes, A.A. Ultra low-cycle fatigue behaviour of a structural steel. *Eng. Struct.* **2014**, *60*, 214–222. [[CrossRef](#)]
7. Jia, L.; Ge, H. *Ultra-Low Cycle Fatigue Failure of Metal Structures under Strong Earthquakes*; Tongji University Press: Shanghai, China, 2018; pp. 1–11.
8. Tian, J.; Wang, X.; Li, H.; Wang, Z.; Pan, J. Ultra-low cycle fatigue performance of grid structure with bolted spherical joints. *J. Constr. Steel Res.* **2023**, *201*, 107728. [[CrossRef](#)]
9. Li, S.; Lin, J.; Zhuge, H.; Xie, X.; Cheng, C. Ultra-low cycle fatigue fracture initiation life evaluation of thick-walled steel bridge piers with microscopic damage Index under bidirectional cyclic loading. *Structures* **2022**, *43*, 669–681. [[CrossRef](#)]
10. Kermajani, M.; Malek Ghaini, F.; Miresmaeili, R.; Aghakouchak, A.A.; Shadmand, M. Effect of weld metal toughness on fracture behavior under ultra-low cycle fatigue loading (earthquake). *Mater. Sci. Eng. A Struct. Mater. Prop. Microstruct. Process.* **2016**, *668*, 30–37. [[CrossRef](#)]
11. Lavogiez, C.; Dureau, C.; Nadot, Y.; Villechaise, P.; Hemery, S. Crack initiation mechanisms in Ti-6Al-4V subjected to cold dwell-fatigue, low-cycle fatigue and high-cycle fatigue loadings. *Acta Mater.* **2023**, *244*, 118–560. [[CrossRef](#)]
12. Li, S.; Xie, X.; Cheng, C.; Tian, Q. A modified Coffin-Manson model for ultra-low cycle fatigue fracture of structural steels considering the effect of stress triaxiality. *Eng. Fract. Mech.* **2020**, *237*, 107–223. [[CrossRef](#)]
13. Anderson, T.L. *Fatigue Mechanics: Fundamentals and Applications*; CRC Press: Boca Raton, FL, USA, 1991.
14. Huang, X.; Yuan, Y.; Zhao, J.; Wei, C. Comparative study on ultra-low-cycle-fatigue behavior of Q235 normal-steel and Q690 high-strength steel. *J. Constr. Steel Res.* **2022**, *194*, 107–308. [[CrossRef](#)]
15. Manson, S.S. Fatigue: A complex subject—Some simple approximations. *Exp. Mech.* **1965**, *5*, 193–226. [[CrossRef](#)]
16. Coffin, C., Jr. A Study of the Effects of Cyclic Thermal Stresses on a Ductile Metal. *Trans. Am. Soc. Mech. Eng.* **1954**, *76*, 931–950. [[CrossRef](#)]
17. Miner, M.A. Cumulative damage in fatigue. *J. Appl. Mech.* **1945**, *67*, 159–164. [[CrossRef](#)]
18. Kuwamura, H. Transition between Fatigue and Ductile Fracture in Steel. *J. Struct. Eng.* **1997**, *123*, 864–870. [[CrossRef](#)]
19. Huang, X.; Zhang, X.; Miao, T. Damage prediction model for ultra-low cycle fatigue fracture failure of structural steel for buildings. *Eng. Mech.* **2017**, *34*, 101–108.
20. Pereira, J.C.R.; De Jesus, A.M.P.; Fernandes, A.A. A new ultra-low cycle fatigue model applied to the X60 piping steel. *Int. J. Fatigue* **2016**, *93*, 201–213. [[CrossRef](#)]
21. Xue, L. A unified expression for low cycle fatigue and extremely low cycle fatigue and its implication for monotonic loading. *Int. J. Fatigue* **2008**, *30*, 1691–1698. [[CrossRef](#)]
22. Xue, L. Damage accumulation and fracture initiation in uncracked ductile solids subject to triaxial loading. *Int. J. Solids Struct.* **2007**, *44*, 5163–5181. [[CrossRef](#)]
23. Pereira, J.C.R.; Wittenberghe, J.V.; Jesus, A.; Thibaux, P.; Fernandes, A.A. Ultra-Low-Cycle Fatigue Behavior of Full-Scale Straight Pipes Under Alternating Bending. In Proceedings of the ASME 2016 Pressure Vessels and Piping Conference, Vancouver, BC, Canada, 17–21 July 2016.
24. Mortezaigholi, M.H.; Zahrai, S.M. Evaluating ultra low cycle fatigue based on ductile fracture model in double core BRBs. *Eng. Struct.* **2020**, *223*, 111–158. [[CrossRef](#)]
25. McClintock, F.A.; Kaplan, S.M.; Berg, C.A. Ductile fracture by hole growth in shear bands. *Int. J. Fract. Mech.* **1966**, *2*, 614–627. [[CrossRef](#)]
26. McClintock, F.A. Erratum: “A Criterion for Ductile Fracture by the Growth of Holes” (*Journal of Applied Mechanics* **1968**, *35*, 363–371). *J. Appl. Mech.* **1968**, *35*, 617. [[CrossRef](#)]
27. Rice, J.R.; Tracey, D.M. On the ductile enlargement of voids in triaxial stress fields\*. *J. Mech. Phys. Solids* **1969**, *17*, 201–217. [[CrossRef](#)]
28. Kiran, R.; Khandelwal, K. A micromechanical model for ductile fracture prediction in ASTM A992 steels. *Eng. Fract. Mech.* **2013**, *102*, 101–117. [[CrossRef](#)]
29. Kiran, R.; Khandelwal, K. A micromechanical cyclic void growth model for ultra-low cycle fatigue. *Int. J. Fatigue* **2015**, *70*, 24–37. [[CrossRef](#)]
30. Hancock, J.W.; Mackenzie, A.C. On the mechanisms of ductile failure in high-strength steels subjected to multi-axial stress-states. *J. Mech. Phys. Solids* **1976**, *24*, 147–160. [[CrossRef](#)]
31. Kanvinde, A.M.; Deierlein, G.G. The Void Growth Model and the Stress Modified Critical Strain Model to Predict Ductile Fracture in Structural Steels. *J. Struct. Eng.* **2006**, *132*, 1907–1918. [[CrossRef](#)]
32. Yin, F.; Yang, L.; Wang, M.; Zong, L.; Chang, X. Study on ultra-low cycle fatigue behavior of austenitic stainless steel. *Thin-Walled Struct.* **2019**, *143*, 106–205. [[CrossRef](#)]
33. Myers, A.T.; Kanvinde, A.M.; Deierlein, G.G. Calibration of the SMCS Criterion for Ductile Fracture in Steels: Specimen Size Dependence and Parameter Assessment. *J. Eng. Mech.* **2010**, *136*, 1401–1410. [[CrossRef](#)]
34. Yin, F.; Yang, L.; Zong, L.; Liu, X.; Wang, Y. Ultra-low Cycle Fatigue Fracture of High-Strength Steel Q460C and Its Weld. *J. Mater. Civ. Eng.* **2018**, *30*, 04018280.1–04018280.16. [[CrossRef](#)]
35. Chang, X.; Yang, L.; Zong, L.; Zhao, M.H.; Yin, F. Study on cyclic constitutive model and ultra low cycle fracture prediction model of duplex stainless steel. *J. Constr. Steel Res.* **2019**, *152*, 105–116. [[CrossRef](#)]

36. Luo, J.; Li, S.; Mao, L.; Shi, G. Constitutive model of duplex stainless steel S22053 and its weld under cyclic large plastic strain loading. *J. Constr. Steel Res.* **2023**, *205*, 107882. [[CrossRef](#)]
37. Zhang, M.; Zheng, B.; Wang, J.; Wu, B.; Shu, G. Study on fracture properties of duplex stainless steel and its weld based on micromechanical models. *J. Constr. Steel Res.* **2022**, *190*, 107115. [[CrossRef](#)]
38. Kanvinde, A.M.; Deierlein, G.G. Cyclic Void Growth Model to Assess Ductile Fracture Initiation in Structural Steels due to Ultra Low Cycle Fatigue. *J. Eng. Mech.* **2007**, *133*, 701–712. [[CrossRef](#)]
39. Kanvinde, A.M.; Deierlein, G.G.; Kunnath, S.K. Validation of Cyclic Void Growth Model for Fracture Initiation in Blunt Notch and Dogbone Steel Specimens. *J. Struct. Eng.* **2008**, *134*, 1528–1537. [[CrossRef](#)]
40. Myers, A.T.; Kanvinde, A.M.; Deierlein, G.G.; Baker, J.W. Probabilistic Formulation of the Cyclic Void Growth Model to Predict Ultra low Cycle Fatigue in Structural Steel. *J. Eng. Mech.* **2014**, 75–100.
41. Song, F.; Zhang, T.; Xie, X. Effect of Corroded Surface Morphology on Ultra-Low Cycle Fatigue of Steel Bridge Piers. *Materials* **2021**, *14*, 666. [[CrossRef](#)]
42. Wang, Y.M. Influence of Welding Residual Stress on Ultra-Low Cycle Fatigue Properties of Beam-Column Joints in Steel Frame. *Strength Mater.* **2022**, *54*, 734–746. [[CrossRef](#)]
43. Adasooriya, N.D.; Siriwardane, S.C.; Ohga, M. A simplified approach to predict the failure of steel members under interaction effect of fracture and fatigue. *Int. J. Fatigue* **2013**, *47*, 161–173. [[CrossRef](#)]
44. Qiu, C.; Xing, J.; Zhang, L.; Wang, T. Ultra-Low Cycle Fatigue Characteristics of Q460 High Strength Steel and T-Shaped Butt Joints. *J. Vib. Shock* **2021**, *40*, 166–174.
45. Kanvinde, A.M.; Deierlein, G.G. Micromechanical Simulation of Earthquake-Induced Fracture in Steel Structures. Ph.D. Thesis, Stanford University, Stanford, CA, USA, 2014.
46. Liao, F.; Wang, W.; Chen, Y. Parameter calibrations and application of micromechanical fracture models of structural steels. *Struct. Eng. Mech.* **2012**, *42*, 153–174. [[CrossRef](#)]
47. Yin, Y.; Li, S.; Han, Q.; Lei, P. Calibration and verification of cyclic void growth model for G20Mn5QT cast steel. *Eng. Fract. Mech.* **2019**, *206*, 310–329. [[CrossRef](#)]
48. Nascimbene, R. Penalty partial reduced selective integration: A new method to solve locking phenomena in thin shell steel and concrete structures. *Curved Layer. Struct.* **2022**, *9*, 352–364. [[CrossRef](#)]
49. Huang, X.; Wei, C.; Zhou, J.; Zhao, J.; Ge, J. Experimental and numerical study on ultra low cycle fatigue fracture of X steel tubular joints with CHS braces to SHS chord. *Thin-Walled Struct.* **2021**, *162*, 107564. [[CrossRef](#)]
50. Li, S.; Xie, X.; Tian, Q.; Cheng, C.; Zhang, Z. Improved Ultra-Low Cycle Fatigue Fracture Models for Structural Steels Considering the Dependence of Cyclic Damage Degradation Parameters on Stress Triaxiality. *Int. J. Steel Struct.* **2021**, *21*, 329–348. [[CrossRef](#)]
51. Li, S.; Xie, X.; Tian, Q.; Zhang, Z.; Cheng, C. A proposal on ultra-low cycle fatigue damage evaluation of structural steels. *Theor. Appl. Fract. Mech.* **2021**, *114*, 102973. [[CrossRef](#)]
52. Gurson, A.L. Continuum Theory of Ductile Rupture by Void Nucleation and Growth: Part I—Yield Criteria and Flow Rules for Porous Ductile Media. *J. Eng. Mater. Technol.* **1977**, *99*, 2–15. [[CrossRef](#)]
53. Rudnicki, J.W.; Rice, J.R. Conditions for the localization of deformation in pressure-sensitive dilatant materials. *J. Mech. Phys. Solids* **1975**, *23*, 371–394. [[CrossRef](#)]
54. Yamamoto, H. Conditions for shear localization in the ductile fracture of void-containing materials. *Int. J. Fract.* **1978**, *14*, 347–365. [[CrossRef](#)]
55. Tvergaard, V. Influence of voids on shear band instabilities under plane strain conditions. *Int. J. Fract.* **1981**, *17*, 389–407. [[CrossRef](#)]
56. Tvergaard, V. On localization in ductile materials containing spherical voids. *Int. J. Fract.* **1982**, *18*, 237–252. [[CrossRef](#)]
57. Tvergaard, V. Material failure by void coalescence in localized shear bands. *Int. J. Solids Struct.* **1982**, *18*, 659–672. [[CrossRef](#)]
58. Tvergaard, V.; Needleman, A. Analysis of the cup-cone fracture in a round tensile bar. *Acta Metall.* **1984**, *32*, 157–169. [[CrossRef](#)]
59. Rakin, M.; Cvijovic, Z.; Grabulov, V.; Putic, S.; Sedmak, A. Prediction of ductile fracture initiation using micromechanical analysis. *Eng. Fract. Mech.* **2004**, *71*, 813–827. [[CrossRef](#)]
60. Mear, M.E.; Hutchinson, J.W. Influence of yield surface curvature on flow localization in dilatant plasticity. *Mech. Mater.* **1985**, *4*, 395–407. [[CrossRef](#)]
61. Steglich, D.; Pirondi, A.; Bonora, N.; Brocks, W. Micromechanical modelling of cyclic plasticity incorporating damage. *Int. J. Solids Struct.* **2005**, *42*, 337–351. [[CrossRef](#)]
62. Huang, X.; Tong, L.; Zhou, F.; Chen, Y. Prediction of fracture behavior of beam-to-column welded joints using micromechanics damage model. *J. Constr. Steel Res.* **2013**, *85*, 60–72. [[CrossRef](#)]
63. Wang, J.; Zhuo, Z. Evaluation of fracture performance of Q690 steel and its welded joints based on GTN damage model. *Chin. J. Ship Res.* **2022**, *17*, 142–147.
64. Oh, Y.; Nam, H.; Kim, Y.; Miura, N. Application of the GTN model to ductile crack growth simulation in through-wall cracked pipes. *Int. J. Press. Vessel. Pip.* **2018**, *159*, 35–44. [[CrossRef](#)]
65. Li, X.; Chen, Z.; Dong, C. Size effect on the damage evolution of a modified GTN model under high/low stress triaxiality in meso-scaled plastic deformation. *Mater. Today Commun.* **2021**, *26*, 101782. [[CrossRef](#)]

66. Qiang, B.; Wang, X. Ductile crack growth behaviors at different locations of a weld joint for an X80 pipeline steel: A numerical investigation using GTN models. *Eng. Fract. Mech.* **2019**, *213*, 264–279. [[CrossRef](#)]
67. Ishida, T. Acoustic emission monitoring of hydraulic fracturing in laboratory and field. *Constr. Build. Mater.* **2001**, *15*, 283–295. [[CrossRef](#)]
68. Yu, M.; Xie, X.; Li, S. A Simplified Ductile Fracture Model for Predicting Ultra-Low Cycle Fatigue of Structural Steels. *Materials* **2022**, *15*, 1663. [[CrossRef](#)]
69. Nkoubou Kaptchouang, N.B.; Monerie, Y.; Perales, F.; Vincent, P. Cohesive GTN model for ductile fracture simulation. *Eng. Fract. Mech.* **2021**, *242*, 107437. [[CrossRef](#)]
70. Liao, F.; Tang, S.; Tu, L. Parameter Calibration of GTN Model for Q460D High Strength Steel and Corresponding ER55-G Welding Material. *J. Xi'an Univ. Archit. Technol.* **2019**, *51*, 695–703.
71. Jia, L.; Ge, H. Ductile Crack Initiation of Structural Steel under Monotonic Loading. In *Ultra-low-Cycle Fatigue Failure of Metal Structures under Strong Earthquakes*; Springer: Singapore, 2018; pp. 53–69.
72. Chaboche, J.L. Anisotropic creep damage in the framework of continuum damage mechanics. *Nucl. Eng. Des.* **1984**, *79*, 309–319. [[CrossRef](#)]
73. Lemaitre, J. A Continuous Damage Mechanics Model for Ductile Fracture. *J. Eng. Mater. Technol.* **1985**, *107*, 83–89. [[CrossRef](#)]
74. Lubliner, J.; Oliver, J.; Oller, S.; Onate, E. A plastic-damage model for concrete. *Int. J. Solids Struct.* **1989**, *25*, 299–326. [[CrossRef](#)]
75. Martinez, X.; Oller, S.; Barbu, L.G.; Barbat, A.H.; De Jesus, A.M.P. Analysis of Ultra Low Cycle Fatigue problems with the Barcelona plastic damage model and a new isotropic hardening law. *Int. J. Fatigue* **2015**, *73*, 132–142. [[CrossRef](#)]
76. Li, S.; Xie, X.; Liao, Y. Improvement of Cyclic Void Growth Model for Ultra-Low Cycle Fatigue Prediction of Steel Bridge Piers. *Materials* **2019**, *12*, 1615. [[CrossRef](#)] [[PubMed](#)]
77. Xiang, P.; Qing, Z.; Jia, L.; Wu, M.; Xie, J. Damage evaluation and ultra-low-cycle fatigue analysis of high-rise steel frame with mesoscopic fracture models. *Soil Dyn. Earthq. Eng.* **2020**, *139*, 106283. [[CrossRef](#)]
78. Tian, Q.; Zhuge, H.; Xie, X. Prediction of the Ultra-Low-Cycle Fatigue Damage of Q345qC Steel and its Weld Joint. *Materials* **2019**, *12*, 4014. [[CrossRef](#)] [[PubMed](#)]
79. Bonora, N. A nonlinear CDM model for ductile failure. *Eng. Fract. Mech.* **1997**, *58*, 11–28. [[CrossRef](#)]
80. Tian, Q.; Liao, Y.; Xie, X.; Zhuge, H. Study on the Prediction Method of the Ultra-Low-Cycle Fatigue Damage of Steel. *Appl. Sci.* **2020**, *10*, 679. [[CrossRef](#)]
81. Liao, F.; Wang, W.; Chen, Y. Prediction of Ultra-Low Cycle Fatigue Fracture of Steel Structure Joints under Reversed Loading. *J. Tongji Univ. (Nat. Sci. Ed.)* **2014**, *42*, 539–546, 617.
82. Smith, C.M.; Deierlein, G.; Kanvinde, A.M. *A Stress-Weighted Damage Model for Ductile Fracture Initiation in Structural Steel under Cyclic Loading and Generalized Stress States*; ProQuest Dissertations Publishing, John A. Blume Earthquake Engineering Technical Report 187; Stanford Digital Repository: Stanford, CA, USA, 2014.
83. Smith, C.; Ziccarelli, A.; Terashima, M.; Kanvinde, A.; Deierlein, G. A stress-weighted ductile fracture model for steel subjected to Ultra Low Cycle Fatigue. *Eng. Struct.* **2021**, *245*, 112964. [[CrossRef](#)]
84. Zhu, Y.; Fell, B.; Kanvinde, A. Continuum damage mechanics based ductile fatigue-fracture prediction in buckling steel braces. *J. Constr. Steel Res.* **2021**, *184*, 106812. [[CrossRef](#)]
85. Di, Y.; Novokshanov, D.; Münstermann, S. Safety assessment of steels under ULCF loading conditions with damage mechanics model. *Procedia Struct. Integr.* **2016**, *2*, 632–639. [[CrossRef](#)]
86. Liu, Y.; Jia, L.; Ge, H.; Kato, T.; Ikai, T. Ductile-fatigue transition fracture mode of welded T-joints under quasi-static cyclic large plastic strain loading. *Eng. Fract. Mech.* **2017**, *176*, 38–60. [[CrossRef](#)]
87. Xie, X.; Cheng, C.; Li, S. A Deformation History-Based Approach for Ultra-Low Cycle Fatigue Damage Evaluation of Steel Structures. *Int. J. Steel Struct.* **2020**, *20*, 1378–1392. [[CrossRef](#)]
88. Wang, T.; Wen, J.; Liao, P.; Zhang, X.; Kim, Y.; Tu, S. A study of ultra-low cycle fatigue failure based on a fracture strain energy model. *Int. J. Fatigue* **2021**, *146*, 106149. [[CrossRef](#)]

**Disclaimer/Publisher's Note:** The statements, opinions and data contained in all publications are solely those of the individual author(s) and contributor(s) and not of MDPI and/or the editor(s). MDPI and/or the editor(s) disclaim responsibility for any injury to people or property resulting from any ideas, methods, instructions or products referred to in the content.